THESIS

CHARACTERISTICS OF GAMMA RADIATION FIELDS IN SUBTERRANEAN STRUCTURES FOR RADIATION PROTECTION AND DECISION MAKING

Submitted by

Alex R. Parker

Department of Environmental and Radiological Health Sciences

In partial fulfillment of the requirements

For the Degree of Master of Science

Colorado State University

Fort Collins, Colorado

Summer 2022

Master's Committee:

Advisor: Alexander Brandl

Thomas E. Johnson
James Lindsay

ABSTRACT

CHARACTERISTICS OF GAMMA RADIATION FIELDS IN SUBTERRANEAN STRUCTURES FOR RADIATION PROTECTION AND DECISION MAKING

The threat of a CBRN attack or accident within subterranean space presents unique challenges for decision makers and emergency planners due to the operational constraints imposed by the physical environment. Radiological exposure device threat scenarios have not previously been explored for vulnerable subsurface infrastructure, like mass transit tunnels. It is important to investigate the impact that radiation exposure devices could have in these types of environments because radiation fields from gamma ray emitting sources behave peculiarly in well shielded and confined spaces where radiation scattering is substantial. This project began with benchmark measurements of a Cs-137 source in several different well shielded, small scale tunnel geometries as a proof of concept study demonstrating the complexity of radiation fields in such environments. Follow on calculations utilizing the radiation transport code, MCNP®, confirmed that the high scattering environment results in apparent radiation streaming down the length of the tunnel, where the calculated dose rates are higher than observed in a free field at equivalent distances. The tunnel material also proved important for the impact of radiation scattering, implying that there is an optimization between the probability of scattering and self-absorption in walls. Other simulated tunnel geometries confirmed the presence of scatter and increased radiation dose rates beyond the line-of-sight of the source, where virtually no transmission is expected through the tunnel

materials. The final part of this project was implementing the modeling techniques into real world threat scenarios for subterranean infrastructure. Two models of a full sized underground roadway were completed using two known radiological exposure device threat materials, Cs-137 and Co-60. Both models resulted in similarly shaped radiation fields and confirmed that the near wall of a crossing roadway offered lower radiation dose rates than the far wall upon approach. These findings could prove useful to decision makers facing a subsurface infrastructure CBRN incident and could lead to the development of tools that can be implemented into emergency preparedness framework.

ACKNOWLEDGEMENTS

I would like to thank my advisor, Dr. Alex Brandl, for welcoming me to Colorado State University and for fostering a positive research group climate in which I always felt comfortable. Traveling to Austria with Dr. Brandl was a highlight of my time at CSU and I look forward to fostering the connections I have made as a result, especially Obst. Peter Hofer and the NIKE research group. The data gathered while in Austria was made possible by the hospitality and support provided during our time at ABCAbwz Korneuburg, most notably from Peter Mohr and Michael Schrenk. I am grateful to have had the opportunity to work on a project that extends beyond the CSU campus laboratories, and I am excited to see what the future of the project holds.

I would also like to express my gratitude to the ERHS faculty that successfully adapted the classroom despite the constraints imposed by a global pandemic. I was perpetually impressed by the quality of instruction, especially by Dr. Brandl, Dr. Johnson and Dr. Sudowe. My ‘COVID Classmates’ (Maëlle, Michaella, Nicole and Yuiko) made graduate school during lockdowns bearable and I am proud of the way we helped each other grow and succeed. For the technical aspects of the project, I am appreciative of all the support provided by the Silver Fir Software team, especially Greg, Andy and John. I am also thankful for the technical support provided by fellow graduate student, Dave Oertli, who made the computational endeavors of this project possible.

Finally, I would like to thank my wife, Candice, for her unwavering support of my endeavors and for giving me the space I needed to work in my own way. It is my hope that Candice and our son, Alton, will look upon my work with proud eyes.

TABLE OF CONTENTS

INTRODUCTION

Subsurface Structures

Subterranean structures have become ubiquitous in urban environments and their use has continued to grow. Urban sprawl over the last century has created more demand for public transportation and other infrastructure that is often built underground due to space constraints. Even rural environments have seen increases in subsurface infrastructure, as it becomes more efficient to blast and drill through a mountain range rather than build a pass over it. Subterranean construction is great for public infrastructure and quality of life; however, it introduces new challenges for emergency response or military operators. One especially important challenge is response to a chemical, biological, or radiological accident or attack in subsurface infrastructure. As these structures grow in number and population density, it is important to investigate vulnerabilities and understand how to best approach complex emergency scenarios.

Subterranean infrastructure varies in use, but it is commonly established in high population density areas where land is at a premium. Subsurface mass transit systems are found in most major cities across the globe, with few cities opting for above ground light rail. The sprawling tunnel systems required for effective public transportation create a labyrinth of tunnels that range from pedestrian walkways to large stations with multiple light rail tracks. In addition to pedestrian walkways and light rail, subterranean infrastructure can also include parking garages, retail shopping, or even repurposed bomb shelters. (Bogan, 2020)

In rural environments, subterranean infrastructure is often created as the most efficient means of navigating geographical obstacles, like mountains or bays. Although not quite as dense as urban mass transit, traffic congestion can cause some rural tunnels to become dense with travelers. Some tunnels, like the well-known Channel Tunnel connecting the UK and France, are designed for both auto transportation and rail transportation. With improved technology, nations are now able to build longer, more ambitious tunnels that bore through mountain ranges or under lakes. The current longest road tunnel in the world, the Laerdal Tunnel in Norway, is 24.5 km long and was completed in the year 2000. (VisitNorway, 2022) The longest rail tunnel in the world is the Gotthard Base Tunnel in Switzerland stretching 57.1 km through the Alps. (AlpTransit, 2010) These long tunnels are often built through mountains or underwater, where it is difficult to incorporate additional egress or access points along the tunnel length. With increasing tunnel lengths, additional considerations are required for safe and secure daily operation.

Due to the abundance of vulnerable underground infrastructure across the European continent, an interdisciplinary research group called 'NIKE' (Nachhaltige Interdisziplinarität bei Komplexen Einsätzen unter Tage or sustainable interdisciplinarity in complex subsurface operations) was established to address many of the challenges faced when operating in subterranean environments. The interdisciplinary NIKE group spans many lines of effort with collaboration between several military and civilian organizations. The primary goal of the collaborative group is to develop and validate **S**afety and **S**ecurity **S**trategies for **S**ub**S**urface **S**tructures or the S-6 model. (Hofer, 2019) This study aims to demonstrate that gamma radiation fields are more complex and less

predictable in well shielded environments than in free air. In addition, we predict that radiation scatter in subsurface tunnels leads to radiation streaming and increased radiation dose rates beyond direct irradiation from a gamma source. The findings will support the S-6 model and inform CBRN response guidance developed by the NIKE research group.

Exploitations

Subsurface infrastructure, like mass transit in a large metropolis, is a vulnerable or “soft” target due to the physical constraints of the structures. These physical constraints can be exploited to cause disproportionate harm thus requiring special emergency response considerations. The construction of new subterranean infrastructure must design structures that address many different challenges including wireless communications, ventilation, lighting, ingress/egress, fire protection, and basic security of life and property.

Wireless communications are largely dependent on line-of-sight, which is all but lost in subsurface structures, especially long transit tunnels. Modern tunnels are designed so that commuters can maintain a wireless signal and these networks are crucial for emergency response personnel that otherwise rely on line-of-sight handheld radios. Tunnels that are constructed with relays for wireless signal might offer first responders or military operators an opportunity to resume communications with limited interruption; however, it may not be economically feasible to construct such arrays in some tunnel systems.

Another operational constraint in subterranean structures is air quality. Whether it is an underground pedestrian walkway, subway station, or mining gallery, air quality is

negatively impacted by natural and manmade pollutants. Unlike the modern issue of wireless signal, ventilation has long been a critical design element for subterranean structures due to the known hazards associated with mining. One of the first comprehensive works on mining was published in Latin in 1556 by a German academic named Georgius Agricola. In his work, *De Re Metallica*, Agricola formally introduced methods of ventilation and stated “miners are sometimes killed by the pestilential air that they breathe”. (Agricola, 2014) Prior to the publication of Agricola’s collection of 12 volumes in 1556, there was very little in written history about the technical aspects of mining. This ‘pestilential air’ mentioned in Book 1 of 12 was of course referring to the various pollutants in mining galleries or the displacement of breathable oxygen which resulted in illness or death of miners. The air quality hazards present in a given mine are dependent on the purpose and mineral content of the mine. The contaminants in a subsurface atmosphere can be acutely hazardous or they can be carcinogenic, increasing the likelihood of latent health effects. The deadliest contaminant in mining galleries has historically been methane gas that accumulates in coal mines and can explode. With improved ventilation and monitoring, methane explosions have become less common and some focus has shifted to other contaminants with more subtle impacts to public health. Radon gas is a ubiquitous radioactive contaminant that emanates from the earth at a rate dependent on the uranium concentration and permeability of the rock in any given locale. Exposure to radon gas is known to increase the risk of developing lung cancer and has been extensively studied in uranium mine workers. (McPherson, 2009) Air quality concerns and the need for ventilation extend beyond just the mining industry. Transportation tunnels require robust ventilation in order to remove internal combustion

motor exhaust pollutants and to prevent smoke from filling the breathable atmosphere in the event of a fire. Without adequate ventilation, personnel operating in subterranean spaces face additional constraints, like operating with supplied air or a self-contained breathing apparatus.

Subterranean structures generally have few entry or exit points which are carefully positioned to maximize egress in the event of an emergency. These physical access constraints pose a defining challenge for military operations in subterranean environments. Freedom of maneuver is paramount to the success of kinetic military operations; therefore, operating in subsurface structures increases operational risk. Long tunnels traversing difficult terrain offer limited access to targets or hazards within providing only few routes of approach. In addition to the challenges faced by military operators, these constraints make evacuation and emergency response more complex. A simple auto accident could result in a dangerous and complex scenario where routes of egress are blocked, and immediate danger arises from fires or other hazardous materials in transport.

Fires or other hazardous material releases can drastically increase the complexity of an incident in subsurface infrastructure. With limited evacuation routes and little to no natural ventilation, fires can quickly consume breathable oxygen and cause increased harm to occupants. Modern tunnels are designed with many features to improve the safety of those occupying underground spaces like improved ventilation, fire extinguishers, safety corridors with fire rated doors and more. These fire safety features can be beneficial for a broad spectrum of less common accident scenarios like chemical, biological, radiological, or nuclear incidents.

CBRN Threat

Subterranean public transit is a highly attractive target for attackers and the knowledge required for the realization of a technically sophisticated attack can be assumed to exist; therefore, it is necessary to characterize and prepare for such events. (Fischer & Pelzer, 2015) Chemical, Biological, Radiological and Nuclear (CBRN) weapons are generally grouped together for their unconventional nature, despite each having unique properties and consequences. Incident response after the use of a CBRN weapon by first responders or military personnel is inherently complex and the constraints of subsurface infrastructure can further complicate the situation.

Chemical weapons have historically been used by both state and non-state actors. The modern iteration of these unconventional weapons infamously made their dramatic debut on the symmetric, trench scarred battlefields of World War I. State actors on both sides of the conflict made use of these newly developed weapons, attempting to break the stalemate of trench warfare with little success. The first chemical munitions used on the battlefields of Europe were primitive, with some released from their canisters to be carried by the wind rather than fired from howitzers. Since the end of the Great War, various types of more sophisticated chemical weapons have been employed for use against individual targets and indiscriminately against populations. Non-state actors have demonstrated access to chemical weapons and knowledge of their use. In 1995, sarin gas was indiscriminately released underground in the highly populated Tokyo Metro by men from a Japanese domestic terror group. (Smithson, 2000) This attack highlighted a lack of preparedness by emergency response personnel and displayed how the effects of CBRN weapons can be exacerbated in subsurface infrastructure.

Biological weapons have been used throughout recorded history with varying levels of sophistication. Early forms of biological warfare included tipping arrows with substances that encouraged infection in their targets or, more deceivingly, the exchange of goods known to be infected with a pathogen. The major conflicts of the 20th century encouraged the modern development of biological weapons by world powers. Advanced research facilities for biological weapons have high level security, but insider threats are difficult to protect against. In 2001, a Department of Defense scientist working at Fort Detrick used his access to dangerous biological agents to carry out a biological attack. He mailed letters addressed to various media outlets and members of congress that were contaminated with anthrax, resulting in 5 deaths. (FBI.gov, 2016) Biological warfare is known to have a very high potential impact with low-tech, low cost options available to hostile non-state actors. High density public transport is an attractive target for such attacks since the environment is favorable for the transmission of pathogens amongst populations. It is important to evaluate the impact of such attacks and analyze how modern design features in subterranean infrastructure, like modern ventilation, can be used to mitigate the impact of biological weapons.

Radiological and nuclear weapons have both seen less frequent use, largely due to the technical sophistication required and the global ramifications if used. Nuclear devices are extremely difficult for non-nuclear, non-state actors to obtain, but the magnitude of potential detriment is large enough that the overall risk remains high enough to warrant diligence by state actors. Nuclear weapons create enormous kinetic energy via the fission of large nuclei, like uranium 235, and can cause widespread devastation to populations and infrastructure. Common threat scenarios do not necessarily include the

detonation of a nuclear device in subsurface infrastructure since greater effect can be achieved elsewhere. Radiological devices differ from nuclear devices in that they do not rely on explosive energy to cause damage. Radiological weapons use radioactive material to expose populations to radiation which could result in acute or latent health effects. In general, it is widely understood that the psychological toll on the public would likely far exceed the acute damage inflicted by a radiological weapon. Although the fear associated with radiation exposure is not typically commensurate with the reality of the danger, radiological weapons still warrant analysis. In 2006, former KGB and FSB agent, Alexander Litvinenko, was assassinated by ingesting a lethal dose of polonium 210 that was added to his tea. Polonium 210 is an alpha particle emitting radionuclide that can be lethal in very small quantities if ingested. Litvinenko suffered acute radiation syndrome for just over three weeks before succumbing to multiple organ failure. (Owen, 2016) This brazen attack on UK soil reinvigorated efforts to prepare for a radiological incident and reminded the public of the threats that exist.

There are two major categories of radiological weapons, radiological dispersal devices and radiological exposure devices. Radiological dispersal devices (RDDs) are designed in conjunction with conventional explosives to disperse radioactive materials across a large area. Dispersed radioactive material contaminates the surrounding area which can lead to public exposures. Despite the potential for widespread contamination, it would take an enormous amount of radioactive material to cause acute harm to the public. In addition, the kinetic action of the device used to disperse the material makes the danger clear to bystanders, thus alerting them to evacuate the area. Since large enough quantities of dispersible radioactive material are challenging to obtain, fear is the

true desired effect of using an RDD. Victims in the vicinity of an RDD detonation can be evacuated away from the site; therefore, the radiation hazard only persists if the radioactive material is internalized or contaminates the skin. The sarin gas attack on the Tokyo Metro proved that subterranean mass transit is an attractive target for terrorism and the public reaction to such an attack could have global ramifications. Table 1 provides a list compiled from Department of Defense publication JP 3-11 of common radionuclides of concern. (DOD, 2018)

Table 1. Select radionuclides of interest consolidated from Department of Defense Joint Publication 3-11

Name	Symbol	Use
Potassium-40	K-40	Terrestrial
Phosphorus-32	P-32	Atmospheric
Carbon-14	C-14	Atmospheric
Tritium	H-3	Atmospheric, Military
Cobalt-60	Co-60	Industrial, Medical, Military
Cesium-137	Cs-137	Industrial, Military
Iridium-192	Ir-192	Industrial, Medical
Uranium	U-234, U-235, U-238	Industrial, Military
Plutonium	Pu-238, Pu-239, Pu-240	Industrial
Radium-226	Ra-226	Industrial, Military
Radon-222	Rn-222	Industrial
Iodine-131	I-131	Industrial, Medical
Strontium-90	Sr-90	Industrial
Molybdenum-99	Mo-99	Medical
Technetium-99m	Tc-99m	Medical
Fluorine-18	F-18	Medical
Thallium-201	Tl-201	Medical
Nickel-63	Ni-63	Military
Americium-241	Am-241	Military
Thorium-232	Th-232	Military

Radiation exposure devices (REDs) are designed to externally expose targets to radiation from a discrete source of radioactive material. Since alpha and beta particles

have very short ranges, it is implied that REDs would be composed of high energy gamma emitting radionuclides. There have been incidents of radiation burns from beta emitting industrial sources, however, these scenarios require very close contact with the radiation source and are not likely the intent of exposure devices. Radioactive materials are used in almost all major industries, meaning that they are accessible when compared to other forms of unconventional weapons. The amount of radioactivity per unit mass of a nuclide is called the specific activity. Most high energy gamma emitting radionuclides have a high specific activity, therefore, only a small amount of material is required to create a high radiation dose rate surrounding the RED. One common industrial radionuclide is cobalt 60, with a specific activity of approximately 1143 Ci/g. Cobalt 60 emits two high energy gamma rays with each decay and has a specific gamma ray constant of 1.29 R/h per Curie at 1 meter. (Johnson, 2017) Combining these two characteristics, only approximately 0.3 grams of cobalt 60 is needed to create a very high radiation area (as defined by 10 CFR 20.1003) in the vicinity of the source. This example illustrates that the physical dimensions of an RED could be extremely small, making it easier to hide in public spaces. One limiting factor to the benefit of public safety is that a lot of high-density material, like lead, would be required to safely transport and position a high activity gamma source, which might be more difficult to conceal.

The threat profile for the use of an RED as a weapon assumes that the assailant has access to large amounts of radioactive material. The International Atomic Energy Agency (IAEA) defines dangerous quantities for relevant radionuclides, also known as D-values, based on the radioactivity required to cause potentially severe deterministic effects. A threshold dose of 1 Gy is often used to represent the onset of deterministic

effects with threshold dose rates depending on the exposed organs. (IAEA, 2006) The list of dangerous quantities includes only those radionuclides with a high enough specific activity to generate 10 mGy/h from a mass less than 10 kg. In addition, radionuclides with very short half-lives are not included since they are not practical for use in an RED.

The likelihood of a radiological weapon being used is low, but there are documented cases of radiation sources being intentionally placed to cause harm. In 2003, a nuclear medicine researcher in China falsified documents to procure an industrial machine containing a large amount of radioactive iridium 192. He then placed the radioactive source above the ceiling panels in the office of a colleague with whom he was feuding. The source was eventually discovered after two months of unexplained symptoms amongst the hospital staff resulting in a reported 75 injuries. (Bland, 2018) A common threat scenario for the use of REDs is the placement of a discrete radiation source in highly populated public transit where many people would indiscriminately be exposed. Subsurface mass transit is an attractive target for this type of attack where long or repeated exposures to a planted device could result in illness or death of commuters along with widespread panic. Despite the rarity of radiological attacks, dangerous quantities of radioactive materials are accessible compared to other forms of unconventional weapons and should be considered in operating procedures for a CBRN environment. Radiological weapons present one of many threat scenarios within the CBRN scope and it is important for planners to understand the complexities associated with operating in such environment.

Photon Interactions and Scatter

Charged particles, such as alpha or beta radiation, rapidly lose their kinetic energy through a series of Coulomb interactions with the surrounding atoms. These Coulomb interactions cause surrounding atoms to ionize as bound electrons are removed from the atom. Since charged particles cause ionizations through Coulomb forces, they are denoted as directly ionizing. Photons, like the gamma-ray photons emitted from a radiological exposure device, do not possess any charge and are therefore not directly ionizing. There are several mechanisms by which photons can interact with matter to create secondary ionizing charged particles. The most important types of photon interactions are coherent scattering, photoelectric absorption, Compton scattering, pair production, and photonuclear reactions. The probability of each interaction type occurring depends on the energy of the incident photon as well as the material properties of the absorber.

Low energy photons can undergo coherent scattering, also known as Rayleigh scattering, where a photon interacts with the electrons of an atom to change direction while retaining virtually all of its energy. Since no energy is transferred to create secondary ionizing particles, this form of scatter does not contribute to radiation dose. Despite not contributing to radiation dose, coherent scattering can have a significant impact on radiation transport and attenuation within an absorber. The probability of scatter increases with the atomic number, Z, of the absorber, and the scattering deflection angle decreases with increasing photon energy, becoming negligible for photons greater than a few hundred keV. For 100 keV photons in a lead absorber, coherent scatter accounts

for approximately 20% of the total attenuation, but quickly decreases with increasing photon energy. (Choppin, 2014)

Photoelectric absorption is an important mechanism in which incident photons transfer all of their energy to an orbital electron in the absorber. (Einstein, 1905a) This interaction dominates for low energy photons and can contribute significantly to radiation dose. When the energy of an incident photon is absorbed, an orbital electron is ejected from the atom with a kinetic energy equal to the incident photon energy less the binding energy of the electron. Once the bound electron is liberated with kinetic energy, it ionizes other atoms along its path through the Coulomb interaction. The photoelectron interaction with other atoms results in the photon energy being ultimately deposited locally where the photoelectric absorption occurred. The ejected electron leaves a vacancy in the orbital of the atom, which is then filled by other available electrons with lower binding energies. When these electrons move to fill the vacancy, characteristic X-rays are released with energy equal to the difference in binding energies for each electron. The fluorescent radiation is typically absorbed locally in the mass or the excess energy can be transferred to electrons of the same atom to produce Auger electrons and create a cascade of orbital vacancies. The cross section or probability of photoelectric absorption occurring is approximately related to Z^4/E^3. Photoelectric absorption dominates the overall attenuation cross section for low energy photons in high Z material, such as lead. Figure 1 is a diagram depicting an incident photon interacting with an orbital electron which is subsequently ejected with kinetic energy.

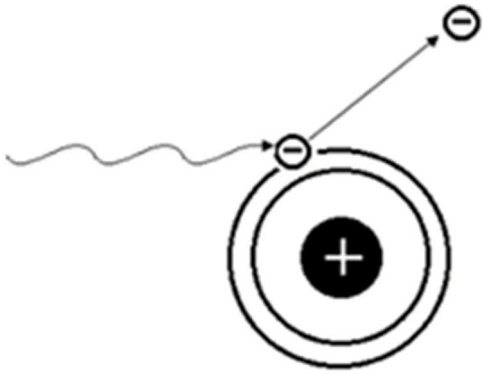

Figure 1. Depiction of an incident photon interacting with an orbital electron via photoelectric absorption

The binding energy of a bound electron, BE, is quantified as energy required to eject a target electron from its orbital and it can be used to determine the resulting kinetic energy of a photoelectron if the incident photon energy is known. The magnitude of the binding energy is dependent on the element and the orbital shell location of the target electron. The energy of an incident photon, E, is proportional to the wavelength, or frequency, f, related by Planck's constant, h, in equation 1:

$$E = hf = h\nu \tag{1}$$

If the incident photon energy and binding energy of the target electron are both known, equation 2 can be used to determine the kinetic energy of an electron ejected via photoelectric absorption (Johnson, 2017):

$$E_{pe} = hf - BE \tag{2}$$

Incoherent scatter, known as Compton scattering, is another interaction mechanism in which photons elastically collide with electrons in the absorber. (Compton, 1923) A portion of the incident photon's momentum and energy are transferred to the target electron, ejecting the electron and changing the direction and wavelength of the

photon. Conservation of momentum dictates that the energy of the incident photon cannot be completely transferred since it would require the electron to eject with a velocity equal to the speed of light in a vacuum. Figure 2 shows how an incident photon can interact resulting in an ejected electron and a scattered photon. (Johnson, 2017)

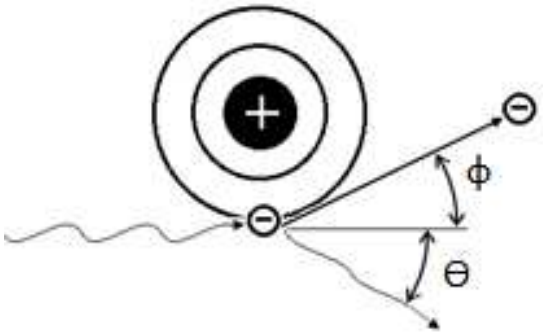

Figure 2. Depiction of an incident photon interacting with an electron via Compton scattering

The angular distribution of the scattered photons follows the well-established Klein-Nishina formula, equation 3 (Knoll, 2010):

$$\frac{d\sigma}{d\Omega} = Zr_0^2 \left(\frac{1}{1+\alpha(1-cos\,\theta)}\right)^2 \left(\frac{1+cos^2\,\theta}{2}\right)\left(1+\frac{\alpha^2(1-cos\,\theta)^2}{(1+cos^2\,\theta)[1+\alpha(1-cos\,\theta)]}\right) \quad (3)$$

Where:

$\frac{d\sigma}{d\Omega} = \text{differential scattering cross section}$

$Z = \text{atomic number}$

$r_0 = \text{classical electron radius}$

$a = \frac{h\nu}{m_e c^2}$ where $m_e c^2$ is electron rest − mass energy

$\theta = \text{scattering angle of incident photon}$

The resulting scattering distribution has an increasing forward tendency with increasing incident photon energy. The amount of energy transferred to the orbital electron is dependent on the scattering angle of the photon, with the maximum energy transfer corresponding to the maximum scattering angle of 180°. The energy of the scattered photon can be calculated using equation 4 if the incident photon energy and scattering angle are known (Knoll, 2010):

$$h\nu' = \frac{h\nu}{1 + \frac{h\nu}{m_e c^2}(1 - cos\,\theta)} \tag{4}$$

Where: $h\nu = \text{photon energy}$

$\theta = \text{photon scattering angle}$

$m_e c^2 = \text{electron rest} - \text{mass energy}$

Photons with energy greater than the rest mass energy of an electron and a positron (1.022 MeV) can undergo another interaction mechanism called pair production. When a high energy photon travels near the nucleus of an atom, the energy of the photon can be transformed into an electron-positron pair. (Blackett & Occhialini, 1933) The first 1.022 MeV of kinetic energy from the photon is transformed into the mass of the two oppositely charged particles and the remaining energy becomes the kinetic energy of the electron and positron. The rest mass of the two particles, m, can be calculated for each using the mass-energy equivalence equation (equation 5) first introduced by Albert Einstein (Einstein, 1905b):

$$E = mc^2 \tag{5}$$

It follows that the total kinetic energy of the two particles, KE_{β^-} and KE_{β^+}, can be calculated using equation 6, with negligible energy lost to the recoiling nucleus nearby (Johnson, 2017):

$$KE_{\beta^-} + KE_{\beta^+} \cong E_\gamma - 2m_e c^2 \quad (6)$$

The charged particles created will lose energy to the surrounding atoms through excitations and ionizations until all of the kinetic energy has dissipated. The positron is of particular interest since it will spontaneously annihilate with an available electron creating two photons with quantized energy equal to the rest mass of an electron (0.511 MeV). The annihilation photons are always present after a pair production interaction occurs and necessarily emit 180 degrees from each other. Figure 3 depicts the incident photon interacting near the atomic nucleus creating two oppositely charged particles with some kinetic energy.

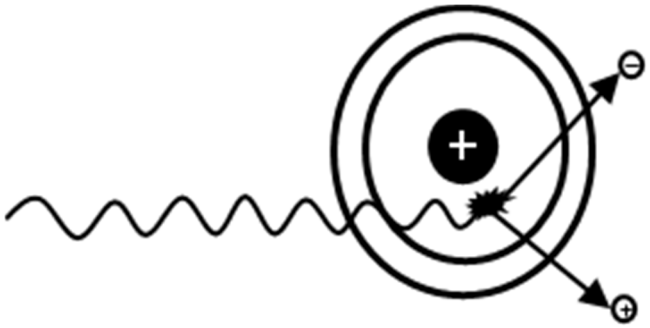

Figure 3. Depiction of an incident photon interacting near the nucleus of an atom via pair production to form two oppositely charged beta particles

Photons with sufficiently high energy can interact with an absorbing medium via photodisintegration to release an energetic neutron from the nucleus of a target atom. This photonuclear reaction requires photon energies greater than the binding energy of

the nucleon, which can vary from about 1.67 MeV up to about 8.5 MeV. Since the photon energy required is high, photodisintegration is typically negligible for most accessible radiation sources and is therefore not considered in the threat scenarios investigated.

Radiation Dose and Dose Rates

Early in the exploration of radiation physics, acute damage, like skin burns or hair loss, was observed following X-ray exposure. Initially, much of the radiation protection concepts were developed to prevent harmful tissue effects since latent effects had not been studied. Observable harmful tissue effects, like erythema, begin to appear once a threshold of radiation dose has been exceeded. Once the threshold dose for tissue damage has been reached, the severity of the damage increases with dose. With the development of the field of health physics, latent health effects were studied to greater extent. Epidemiological studies at higher doses have shown that radiation dose is correlated with increased risk of cancer. Unlike the deterministic effects first explored, latent health effects do not appear to have a radiation dose threshold; however, the no-threshold model is being deliberated in the scientific community due to insufficient evidence at low doses or dose rates. The no-threshold model represents the stochastic hypothesis of latent health effects, that the probability of developing cancer increases with radiation dose and the severity of the cancer is not dependent on radiation dose.

Absorbed dose is the measure of the radiation energy deposited in a given mass. It is a fundamental dose quantity that is useful for understanding thresholds and severity of harmful tissue effects. The SI unit of absorbed dose is the Gray (Gy) and is defined as 1 Joule of absorbed radiation energy per kilogram (1 J/kg). Absorbed dose does not depend on the type of incident radiation and is applicable for both directly and indirectly

ionizing radiation particles. Although the Gray is a useful protection quantity for many deterministic effects, some biological effects of radiation are dependent on the linear energy transfer (LET) of the incident radiation. LET is the measure of the rate of energy transfer along the pathlength of a radiation particle. Alpha particles have a high LET considering their +2 charge and relatively large size, while beta particles have a lower LET. Studies have shown that high LET radiation is more effective at causing biological damage than low LET radiation for the same amount of absorbed dose. The difference in observed biological effects between high and low LET is quantified by a ratio called relative biological effectiveness (RBE), which must be considered when predicting latent radiation effects. (1) In addition, the tissues comprising the human body have varying sensitivities to radiation. Some organs, like the gonads, have a high sensitivity to radiation while others, like the brain, have a lower sensitivity. The law of Bergonié and Tribondeau (1906) states that radiosensitivity of tissue increases for cells that are less differentiated or have high mitotic activity and divide more rapidly. (Hall, 2019)

Effective dose is the resulting dose quantity when both the quality of the radiation in terms of LET and the sensitivity of target tissues are considered. Effective dose is the standard radiation protection dose quantity used to quantify the risk of stochastic effects. Effective dose can be calculated from absorbed dose by using the appropriate radiation and tissue weighting factors. Radiation weighting factors (w_R) account for the comparative biological damage caused by radiation type based on the LET. Tissue weighting factors (w_T) consider the radiosensitivity of the target organs, with the sum of all factors, $\Sigma\, w_T = 1$. The International Commission on Radiological Protection (ICRP) promulgates radiation and tissue weighting factors and publishes updates periodically. Radiation weighting

factors have evolved as more information about the relationship between LET and RBE has been collected. The weighting factor for gamma and beta radiation has remained 1, but the weighting factors for other types of radiation have changed several times, with current recommended weighting factors for neutrons determined using piecewise, energy dependent equations. Since ICRP 26 was published in 1977 (ICRP, 1977), the recommended tissue weighting factors have also been adjusted as new data are collected. The most recent ICRP tissue weighting factors are found in ICRP 103 published in 2007. (ICRP, 2007)

The radiation weighting factor for gamma radiation is equal to the beta radiation weighting factor because gamma radiation energy must be transferred to an electron for any energy to be deposited. Gamma rays must undergo one of the previously described interactions to contribute to absorbed dose in a target. The amount of energy liberated within a given mass is called the kinetic energy released per unit mass or kerma. This unit differs from absorbed dose, which measures the kinetic energy that is locally deposited in the mass. Kerma includes energy that is released within a given mass but may escape the mass prior to depositing additional energy. For the results in this study, the radiation and tissue weighting factors are included and data are reported in effective dose.

Inverse Square Law

The inverse square law describes the relationship between exposure or dose rate and distance from a radiation source. For an isotropic point source, the radiation intensity decreases at a rate equal to the square of the distance from the source. The inverse relationship is easily derived by calculating the surface area of concentric spheres with

varying radii. If the rate of isotropic particle emissions is constant, then the particle fluence decreases with distance as the surface area considered in the fluence increases. This powerful relationship is the reason why distance is considered a main pillar of radiation protection. Equation 7 describes the relationship between radiation intensity, *I*, and distance from an isotropic point source, *d*, in a free field (Johnson, 2017):

$$\frac{I_1}{I_2} = \frac{{d_2}^2}{{d_1}^2} \tag{7}$$

Many real-world sources cannot be approximated as point sources because of their physical dimensions. Large volume sources do not follow the inverse square law in the vicinity of the source. The dose rate from a volume source behaves similarly to a point source at a distance greater than twice the largest dimension of the source. (Johnson, 2017) The inverse square law is commonly used by radiation protection personnel or first responders to calculate characteristics of an encountered radiation source. For high activity gamma sources, the distance to the source can be estimated by taking dose rate measurements at two locations along a path intersecting the source location. Following the inverse square law provided in equation 7, it is expected that the radiation intensity (or dose rate) will decrease by a factor of four if the distance from the source is doubled. For example, if a dose rate of 25 mSv/h is measured then the operator can estimate that they are halfway between the source and the first measurement point when their meter reads 100 mSv/h or 4 times the first measurement. This estimation can be useful for identifying unknown radiation sources and for protecting personnel by establishing appropriate cordons. In environments with high scattering potential or shielding, the inverse square law may not be accurate.

One known example where the inverse square law is invalid is the phenomenon called skyshine. If a gamma radiation source is shielded in a given direction, the photons emitted into the surrounding atmosphere can interact via Compton scattering and be redirected behind the shielding as shown in Figure 4. The resulting radiation dose rate behind the shielding can then be higher than would be predicted if only the transmission through the shielding is considered. In addition, the dose rate behind heavy shielding can increase with distance from the radiation source as favorable scattering angles are achieved. Once the dose rate behind shielding peaks due to scatter, it begins to decrease at a rate somewhere between what is expected for a point source and a planar source. The dose rate in the far field decreases more quickly than the inverse square law predicts (power less than -2) as scatter around the barrier no longer contributes significantly. (Mann, 2018) The importance of this scattering phenomenon is the reason why the positioning of a protective radiation barrier is just as important as the thickness of the absorber material used.

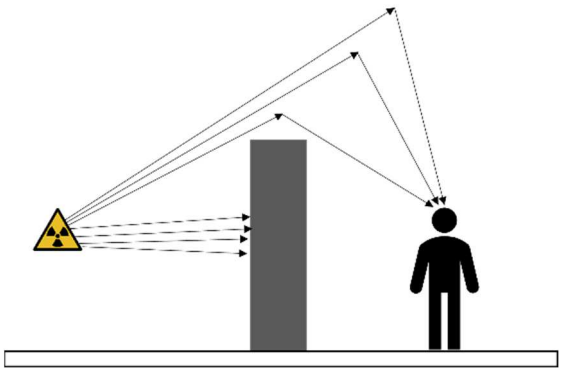

Figure 4. Radiation scattering in air to cause 'skyshine'

Another phenomenon that complicates radiation protection is radiation streaming. Streaming can occur at interfaces of material or through narrow openings where radiation

can traverse the thickness of a barrier with less beam attenuation. Cracks or narrow openings in shielding can lead to a fan-like beam streaming through the absorber material, negating some of the protection factor provided. This phenomenon is the reason why many radiation shielding materials have a ‘tongue and groove’ design to prevent streaming through straight line interfaces between sections. The impact of scatter in gamma radiation environments can be significant and is dependent on both the energy of the photons and material characteristics. It is important for operational planners to understand how high scattering environments can impact response to a radiological event and potentially mislead personnel taking measurements. In the context of force health protection for operators, understanding the behavior of radiation fields within subterranean spaces can optimize movement and protective actions to increase time on station or reduce unit radiation dose.

MCNP®, Attila® and Supporting Software

Mathematicians have explored statistical sampling as a means to solve complex problems many times through history, but it was not until the invention of the first electronic computer that statistical sampling became practical as the process requires enormous computational power to develop enough histories or genealogies to form a statistically valid picture. This became the limiting factor for early development of these methods, until Stanislaw Ulam envisioned a way in which the newly invented ENIAC (Electronic Numerical Integrator and Computer) could be used to complete these tedious calculations in 1945. Ulam’s colleague, John von Neumann, quickly saw the relevance of the revitalized statistical sampling method and outlined a statistical approach for modeling neutron diffusion in fissionable material in 1947. Due to the random outcome of each

event following a probability distribution, it was at this time that the method was called Monte Carlo, after the famous casino in which Ulam's uncle frequently gambled. The combination of Ulam's Monte Carlo method and the ENIAC proved to be powerful as it was used to calculate neutron diffusion problems and proved the feasibility of developing a thermonuclear weapon. (Metropolis, 1987)

When applied to radiation transport problems, the Monte Carlo method involves tracking individual particles as they traverse materials and interact with matter. The probability of interaction within a material is dependent on the material properties, the energy of the particle, and the pathlength through the material. At each material or region interface, the fate of the particle is decided by a roll of the dice, or more precisely, by the selection of a random number along a probability distribution which corresponds to some outcome. The probability distributions are developed using known characteristics, such as attenuation coefficients or neutron capture cross sections.

Monte Carlo n-Particle (MCNP®) transport code was developed for nuclear engineers and radiation protection specialists to more easily set up and solve radiation transport problems. The MCNP® software was developed at Los Alamos National Laboratory with new versions released periodically that are more comprehensive and up to date. MCNP® uses input files, also known as input decks, with very specific layouts to create and model radiation transport problems using Monte Carlo methods. Input decks start with a file name followed by the cell cards and surfaces that will bound the problem set. The regions bound by the generated surfaces define cells. Complex materials can be created in MCNP® using standard libraries of material properties. These materials can be tailor made for any specific problem where each cell is assigned a material. All space

must be defined in the geometry of an MCNP® problem; therefore, all generated cells must be assigned a material, and the remainder of the universe can be assigned as void. Once the geometry has been created, source spectra can be defined and positioned as required. Sources can be created as either a point source or as a volume source. (LANL, 2008)

The last information included in an MCNP® input deck are the desired tallies along with their energy response dependencies. There are several tallies that can be recorded in MCNP®, and each has its use depending on the scenario. The F4 tally is commonly used for radiation protection since it reports fluence through the desired cell. The number of histories, or particles, is defined by the user to optimize the statistics against the required computing time. The source activity is scalable by the user since fluence is calculated per particle emitted. Dose quantities of interest can then be calculated using fluence and the appropriate conversion coefficient. The F5 tally is similar to the F4 tally; however, the F5 tally is not assigned to a cell. The F5 tally can be positioned anywhere in the geometry to make a virtual detector with a radius defined by the user. The F5 tally is useful for measuring dose rates at various locations within cells without recreating the geometry. The F8 tally is useful for analyzing the energy distribution of the particles entering the specified cell. The tallies can be modified using energy response functions which are defined by the user.

The output files from MCNP® can be interpreted fundamentally in a text editor, however, there is a lot of information, and it can be difficult to ascertain data of interest. The tally results include a comprehensive analysis in which ten statistical tests are checked.

Creating complex geometries can be extremely tedious using MCNP® and a traditional input deck. Silver Fir Software® developed Attila4MC® (referred to as Attila) to facilitate importing complex geometries from computer aided design (CAD) files into a format compatible with MCNP®. Attila4MC® uses the imported CAD file to create an unstructured mesh of tetrahedral cells filling the geometry. Using the “Elemental Edit” feature of Attila4MC® allows the user to tally fluence through each of the mesh cells to create a heat map of the geometry for enhanced visualization of radiation transport. After the input file is run with MCNP®, an elemental edit output file (EEOUT) is generated. The EEOUT file can be imported into Attila4MC® as a Tecplot file for visualization of the results.

Methods

Benchmark Study with Cs-137 Source

In order to compare and validate the results of radiation transport models, a set of physical benchmark measurements were taken using a handheld radiation detector. The source used for the benchmark measurements was a 28.3 GBq Cs-137 source (SN 0401GN) with a 0.662 MeV gamma emission. The detector used was a handheld Radeye PRD-ER (ThermoFisher Scientific, Waltham, MA) connected to a PC via an infrared data cable. A free air measurement was simulated by placing the detector and source approximately 1 meter off the ground using a wooden frame to minimize scatter or absorption in the supporting structure. Three small scale tunnel geometries were built to represent different tunnel configurations encountered in real world subsurface infrastructure. The first tunnel was a straight tunnel with an internal cross section just large enough to house the handheld detector (Figure 5). The second tunnel was a T-intersection with the crossing tunnel made wider in order to take measurements at both the near and far walls. The third tunnel geometry was a narrow curved tunnel with an approximate centerline radius of 1 meter. The walls and ceiling of the tunnels were composed of lead bricks while the ground of all three tunnels was concrete. For each of the three tunnel geometries, the radiation source was positioned 5 cm inside one of the openings and the detector was placed at several locations of interest in each configuration. (17)

Figure 5. Picture of straight lead tunnel constructed for the benchmark measurements

Recreation of Benchmark Study Using Attila® and MCNP®

Geometries

Once the physical measurements of the benchmark study were established, each of the experimental designs were modeled using SpaceClaim®, Attila® and MCNP®. In order to effectively model the benchmark study, the geometry of each set up was created in SpaceClaim® CAD software. For the free air measurement, a simple 5 m × 5 m × 5 m box was generated to validate the software and reproduce the gamma ray constant for cesium 137. For the straight tunnel, the CAD design included a 120 cm long rectangular tunnel 10 cm wide and 10 cm tall. The side and overhead walls of the tunnel have a thickness of 5 cm. The bottom of the tunnel was left open and the tunnel was placed on a 15 cm thick slab resembling the concrete ground in the benchmark study. A 1 m tall box was placed on top of the slab to be defined as the air surrounding the tunnel as seen in Figure 6.

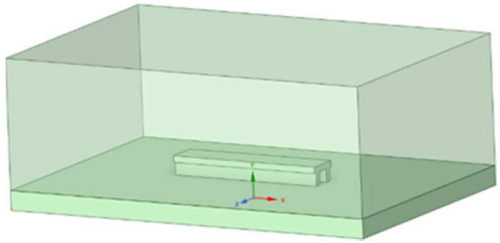

Figure 6. Straight tunnel geometry created in Spaceclaim®

For the T-intersection tunnel, a short tunnel measuring 45 cm in length with a height and width of 10 cm × 10 cm was created joining a crossing tunnel. The crossing tunnel is perpendicular to the short tunnel with a width of 15 cm and a height of 10 cm. All of the tunnel walls have a thickness of 5 cm with the bottom of the tunnel left open for contact with the concrete ground. A 200 cm × 300 cm slab with a thickness of 15 cm was created for the tunnel bottom, representing the concrete ground (Figure 7). A 2 m tall box was placed on top of the slab to define the air surrounding the tunnel.

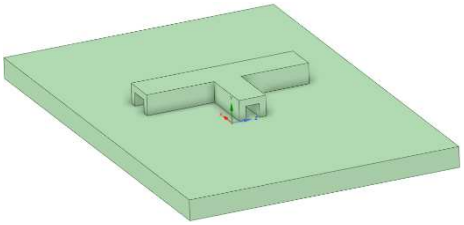

Figure 7. T-intersection tunnel geometry created in Spaceclaim®

The final benchmark study modeled was the curved tunnel. The curved tunnel was created with a centerline radius of 1 m with a width of 10 cm and a height of 10 cm. The sides and top of the tunnel were designed with a thickness of 5 cm to represent the lead bricks used in the benchmark study. Again, the bottom of the tunnel was left open to be placed on a concrete slab. The concreate slab under the curved tunnel was 2 m × 3 m with a thickness of 15 cm (Figure 8). A 2 m tall box was created on top of the slab to represent the air surrounding the tunnel.

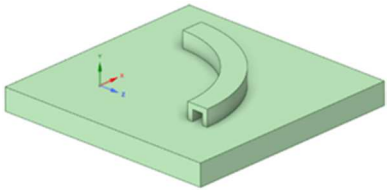

Figure 8. Curved tunnel geometry created in Spaceclaim®

Once the dimensions for each region were established in SpaceClaim®, the CAD models were imported into Attila®. Using Attila®, an unstructured mesh of tetrahedrons, such as presented in Figure 9, was created for each of the models. The overall maximum edge length was set to 0.2 m for all four benchmark models with the ground and tunnel both having a slightly smaller maximum edge length of 0.1 m for increased resolution. These maximum edge lengths were set in accordance with recommendations from Silver Fir Software stating that edge lengths should be approximately 1/20th of the largest model extents.

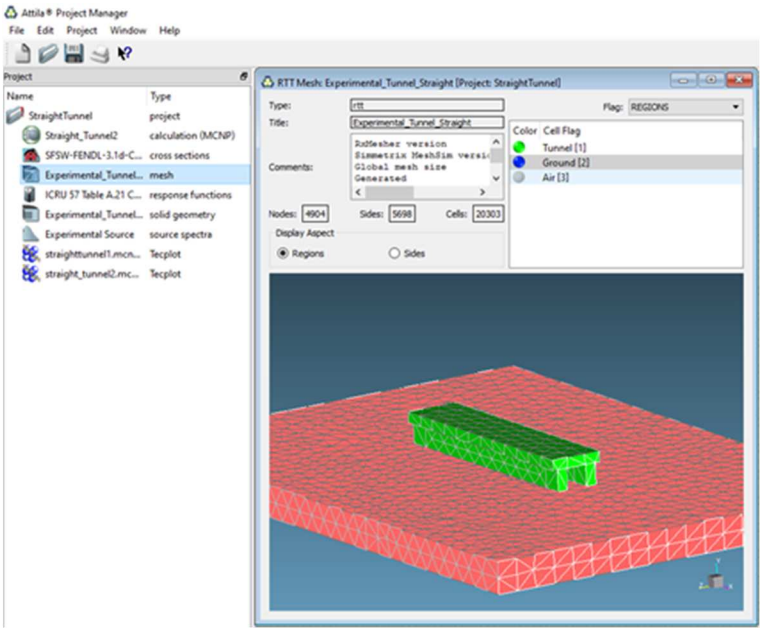

Figure 9. Screenshot from Attila® depicting the unstructured mesh generation of the straight tunnel

The unstructured mesh generated for each model was used as the geometry for the calculations exported to MCNP®. The mesh of cells can be interpreted by MCNP® as independent regions in which photon fluence can be recorded. Within each cell region in the mesh, the fluence can be interpolated so that fluence values can be estimated at any point across the geometry.

MCNP® Calculation Set Up

A source spectrum matching the 0.662 MeV gamma emission of the cesium 137 (Cs-137) source used in the physical benchmark measurement was created in Attila®. In order to define materials within the geometry, the MCNP6 standard library XSmc containing material properties and cross sections was imported into each Attila® calculation set up. The XSmc library contains cross sectional data for both photon and neutron interactions but does not include any multigroup cross section data. Materials containing more than one chemical element can be created manually by adding individual elements and assigning their weight or atom percentage. Once the appropriate weight or atom percentage distribution is defined, the user can then enter the density of the material. These user defined materials then become selectable when assigning the material properties of each cell or region in the calculation. The primary materials used in the benchmark models were air, lead, iron, and concrete. The elemental compositions and densities for each of these materials were set in accordance with the values in a compendium published by PNNL in 2011 (Detwiler, 2021). For air, material number 4 (Air – Dry, Near Sea Level) with a density of 0.0012 g/cm^3 was used. For concrete, material number 97 (Concrete, Ordinary – NIST) with a density of 2.3 g/cm^3 was used. For iron, material number 158 (Iron) with a density of 7.87 g/cm^3 was used. Finally, for lead, material number 171 (Lead) with a density of 11.3 g/cm^3 was used.

Dose response functions are tools in the Attila® framework that can be used to translate tally or elemental edit results into something more useful, such as dose. For this set of calculations, conversion coefficients from ICRU 57, Table A.21 (Appendix A) were utilized. ICRU 57 conversion coefficients relate photon fluence to ambient dose

equivalent, denoted by the H*(10) column. H*(10) represents ambient dose equivalent at a depth of 10 mm, which is an operational quantity used for area monitoring of penetrating radiation, such as high energy gamma radiation. Since these calculations are designed to develop radiation protection recommendations for gamma radiation fields, the H*(10) values were consistently used. Two response functions describing the same ICRU 57 table were required since regular tallies use point-wise functions and elemental edits use group-wise (or constant) functions. The ICRU 57 response generated was established for photon energies between 0 – 10 MeV with interpolation on a linear-log scale as recommended by ICRU. (ICRU, 1998)

For the free air measurement, the Cs-137 source spectrum was assigned to a point source positioned (-50 cm, 0 cm, 0 cm). A 10 cm × 10 cm × 10 cm cube was centered at the position (50 cm, 0 cm, 0 cm) to represent a detector region 1 meter from the source. All space inside the air box was assigned as air, including the source and detector regions. An F4 tally was created in the detector cell with the user generated ICRU 57 response function assigned. An elemental edit function was also generated for visualization of the results. The calculation was run using 100,000,000 particles in order to achieve desirable statistics. Once the calculation was set up in Attila®, it was packed for MCNP® and run.

For the straight tunnel configuration, the Cs-137 source was placed 5 cm inside the opening on one end of the tunnel at position (-55 cm, 20 cm, 0 cm). Since the straight tunnel set up represents the simplest and most foundational geometry for well shielded, subsurface structures, three separate calculations were completed using three different materials. The first straight tunnel calculation was generated to the same specifications

as the benchmark study. In this iteration, the walls and ceilings were assigned lead while the ground was concrete. The remaining space inside the geometry was set to air. The second iteration was identical to the first, except the entirety of the tunnel was defined as concrete instead of lead. For the final calculation, the tunnel walls and ceiling were set to iron, and the ground remained concrete. These three iterations provide a range of densities so that the effect of radiation scatter could be investigated. For all three straight tunnel calculations, 100,000,000 particles were run. Each run included an elemental edit with the user generated ICRU 57 response function for radiation field visualization and measuring fluence (dose) at various positions inside the tunnels.

For the T-intersection tunnel configuration, the Cs-137 source was placed 5 cm inside the narrow tunnel opening at position (-30 cm, 20 cm, 0 cm). This position places the source 40 cm from the opening of the wider crossing tunnel. Two calculations were run for the T-intersection set up. The first iteration consisted of lead tunnel walls and ceiling with a concrete ground. The second iteration was identical to the first except the entire tunnel was made of concrete. For both calculations, the remaining space was filled with air. An elemental edit using the ICRU 57 response function was created for radiation field visualization and for taking measurements at various positions in the crossing tunnel. Each MCNP® calculation was run with 100,000,000 particles.

The final benchmark model to recreate was the curved tunnel. For the curved tunnel, the Cs-137 source was placed 5 cm inside the opening on one end of the tunnel at position (100 cm, 20 cm, 5cm). Only one calculation was performed for the curved tunnel system. The walls and ceiling of the tunnel were assigned as lead while the ground remained concrete as in the previous calculations. An elemental edit using the ICRU 57

response function was created for visualization and analysis of the radiation field. Again, the MCNP® calculation was run with 100,000,000 particles to ensure desired statistical outcomes.

Modeling of Radiation Sources in ZAB Using Attila® and MCNP®

Sections of the Zentrum am Berg (ZAB) facility were previously laser mapped to create an accurate CAD model. The CAD model of the ZAB facility included road, pedestrian, and train tunnels of varying lengths. For this study, a small section of the tunnel system was selected to imitate threat scenarios at positions of interest. The segment of tunnel selected was the two parallel road tunnels with intermittent passageways linking them. For the MCNP® calculations, only two materials were used. Air, as previously defined, filled the space inside the set of tunnels. For the surrounding earth material, limestone (material number 268 in PNNLs compendium) was used, with a density of 2.61 g/cm^3. These two roadways provide an ideal geometry to investigate incidents occurring in road tunnels since the ZAB test and research facility provides real-world dimensions and design features.

Two iterations were completed using the large scale road tunnel from the ZAB facility. Each calculation was completed using a different radionuclide that could potentially be used in a radiological exposure device. The first calculation included a Cs-137 source placed inside a walkway connecting the two road tunnels. This position was selected to maximize the effect of scatter since the connecting walkway is relatively narrow when compared to the full sized road tunnel. The source was placed approximately 10 meters inside one end of the narrow passageway. An elemental edit type tally was created for the entire geometry using the ICRU 57 dose response function

to generate a visualization of the radiation field. Due to the large scale of the road tunnel calculation, 1,000,000,000 particles were run to ensure appropriate statistics. The second calculation was created using Co-60 as the radiation source. Co-60 was selected because it is a commonly used industrial material and it emits two high energy gamma rays per decay. The two gamma ray energies characteristic to Co-60 are 1.173 MeV and 1.332 MeV which contribute to the gamma ray constant, $\Gamma_{Co\text{-}60} = 3.703 \times 10^{-4}$ mSv/h. (Unger & Trubey, 1981) The Co-60 calculation was also run using 1,000,000,000 particles for desirable statistics.

TecPlot360® Visualization

Every calculation completed in MCNP® included an elemental edit tally reporting fluence across the entirety of the geometries. The elemental edit allows for visualization of the radiation fields in three dimensions using Tecplot360®. For each of the small tunnel configurations, the Tecplot360® visualizations were created using the same maximum and minimum values with the same type of color coding. This standardization allows for comparison across the geometries by comparing the resulting heat map coloring. An exponential scale was used for these heat maps in order to distinguish between the lower dose rates that were further from the source.

Benchmark Study Results

The physical benchmark measurements made using the handheld Radeye detector were previously reported. (Parker, 2021) Select data, presented in Table 2, are included here for comparison to calculations made using Attila® and MCNP®. The free air measurement in this benchmark study yielded a dose rate of 2.25 mSv/h at 1 meter. This measurement is 26% less than the predicted dose rate, 3.04 mSv/h at 1 meter calculated using the gamma ray constant for Cs-137. Another measurement was made with the source positioned approximately 5 cm from the asphalt ground with the detector placed 1 meter away on the same plane. This measurement yielded a dose rate of 2.35 mSv/h, which was 4.4% larger than the free air measurement taken 1 meter off of the ground. In addition to the free air measurements, the straight tunnel measurements are included for comparison to the MCNP® calculations.

Table 2. Select data from handheld detector measurements of Cs-137 source

Distance (cm)	*Free Air*	*Free Air (Near Ground)*	*Straight Tunnel*
25	-	-	58.49 mSv/h
50	-	-	12.28 mSv/h
100	2.25 mSv/h	2.35 mSv/h	2.14 mSv/h

MCNP® Models of Benchmark Study Geometries Results

The free air set up was designed to recreate the established gamma constant for Cs-137 in order to validate the material properties and response functions used in subsequent calculations. The F4 tally assigned to the detector cell at 1 meter described earlier yielded 2.96×10^{-5} pSv per particle emitted using the ICRU 57 dose response function. Multiplying the dose per particle by the activity of the source resulted in a dose rate of 3.01 mSv/h with an uncertainty of 0.35%. The output file from this MCNP® calculation is provided in Appendix B for reference. The expected dose rate at 1 meter can be calculated using the gamma ray constant for Cs-137, the distance to the source and the source activity. The source activity used for the calculations was the same as the activity used in the benchmark study, A = 28.3 GBq. The gamma ray constant used for Cs-137 was $\Gamma = 1.075 \times 10^{-4}$ mSv/h per MBq at 1 meter. (Unger & Trubey, 1981) Using these values, the expected dose rate at 1 meter is 3.04 mSv/h. The value calculated using MCNP®, 3.01 mSv/h, is approximately 1% less than the expected value. The high level of agreement between the two values provides confidence in the validity of the subsequent models. The visualization of the free air configuration, Figure 10, depicts an overhead slice of the geometry confirming isotropic emission from the source. The green areas of the image represent the lowest dose rate using the Attila® elemental edit F4 tally across the unstructured mesh. The white area represents the highest dose rate in the image, at the location of the point source.

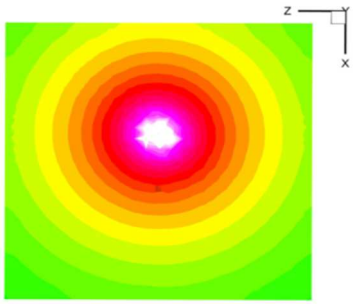

Figure 10. Overhead view of radiation field from Cs-137 point source in air

The straight tunnel model was designed to explore how radiation fields are affected by high scatter environments. The open space of the tunnel also provides an opportunity to investigate radiation streaming along the tunnel length. The first calculation using the straight tunnel configuration was created to replicate the benchmark measurements taken using a handheld detector. In this calculation, the lead tunnel generated a large amount of scatter, resulting in increased dose rates in the near field. Figure 11 is a plot comparing the physical measurements using the handheld Radeye detector to the MCNP® calculation results.

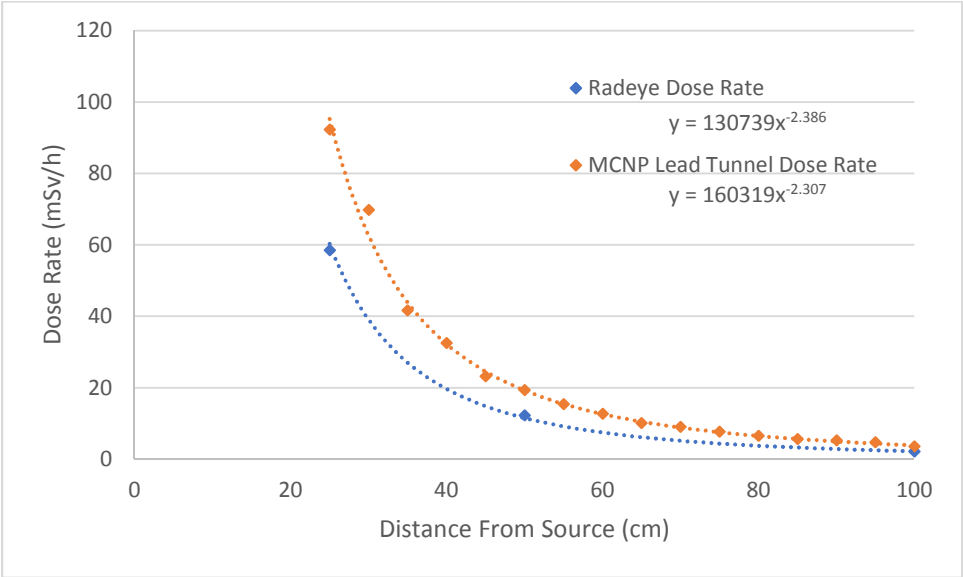

Figure 11. Dose rate comparison between handheld measurements and MCNP® model at various distances

Figure 12 is a plot of dose rate as function of distance from the source both inside the lead tunnel and outside the tunnel in the opposite direction. Comparing the dose rates inside and outside the tunnel allows for analysis of the impact of streaming or scatter inside the tunnel. Outside of the lead tunnel, the dose rate dropped off near the expected rate, following the inverse square law. In this *-x* direction, the only scattering material besides air is the concrete ground 5 cm below the source position. This additional scatter from the ground resulted in higher dose rates per distance than the free air benchmark model. Data points from 10 cm to 95 cm from the source showed a relationship of $r^{-2.05}$ with an R^2 value of 0.996. The radiation field inside of the lead tunnel did not behave according to the inverse square law. Dose rates near the source inside the tunnel were considerably larger than those outside the tunnel. The functional dependency of distance was stronger inside the tunnel with a relationship of $r^{-2.31}$ and $R^2 = 0.976$. Additional data from the straight tunnel geometry are included in Appendix C.

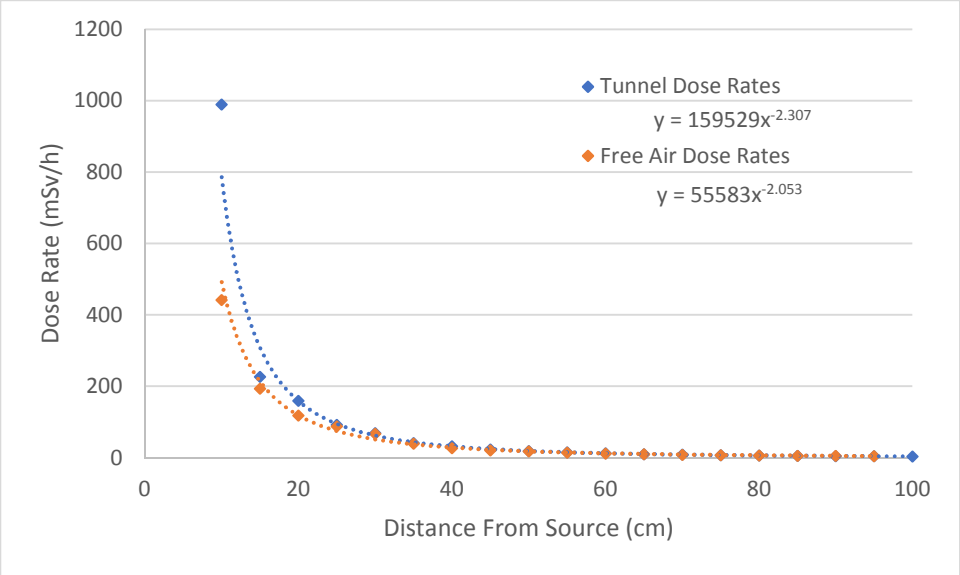

Figure 12. Dose rates both inside and outside (free air) the straight lead tunnel geometry

In the second calculation completed for the straight tunnel, the structure of the tunnel was changed to standard concrete, with a density of 2.3 g/cm^3. Photoelectric absorption is dependent on the atomic number of the target material, therefore, attenuation in the concrete tunnel was significantly different than in the lead tunnel. The dose rate inside the concrete tunnel decreased more quickly than the inverse square law predicts. The functional dependency on distance was $r^{-2.29}$ which was a slightly weaker dependence on distance than observed in the lead tunnel. The dose rate inside the concrete tunnel at 1 meter was approximately 4.03 mSv/h, which is 33% larger than the dose rate calculated at 1 meter in the free air model. The dose rates for both inside the concrete tunnel and outside the tunnel are plotted in Figure 13 with the equations for the lines of fit included.

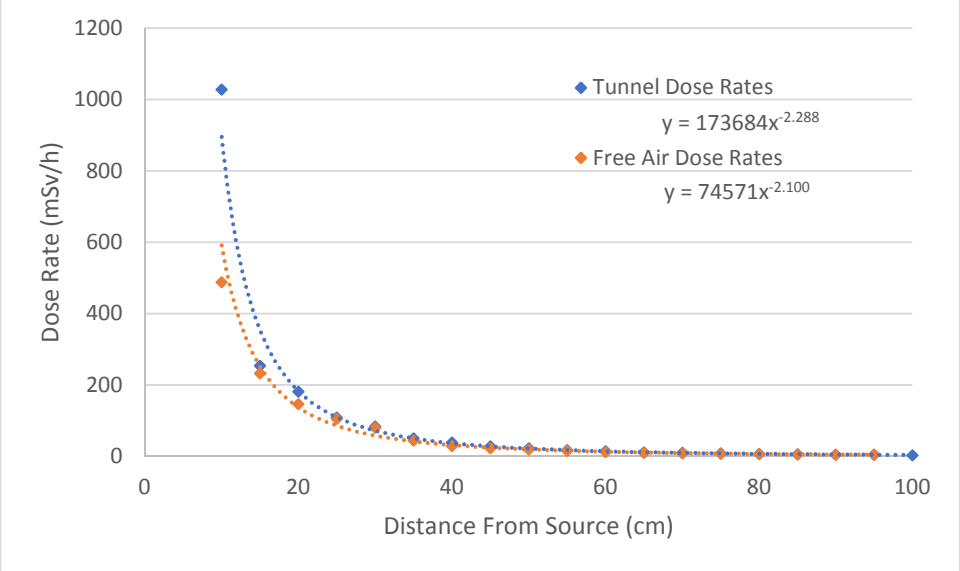

Figure 13. Dose rates both inside and outside (free air) the straight concrete tunnel geometry

To further investigate the impact of scattering within the tunnel structure, the dose rate inside the concrete tunnel was divided into three segments: near field, mid field and

far field. Figure 14 shows the three different regions along with the functional dependence on distance from the source. The relationship between dose rate and distance ranged from $r^{-2.21}$ in the near field to $r^{-2.53}$ in the far field.

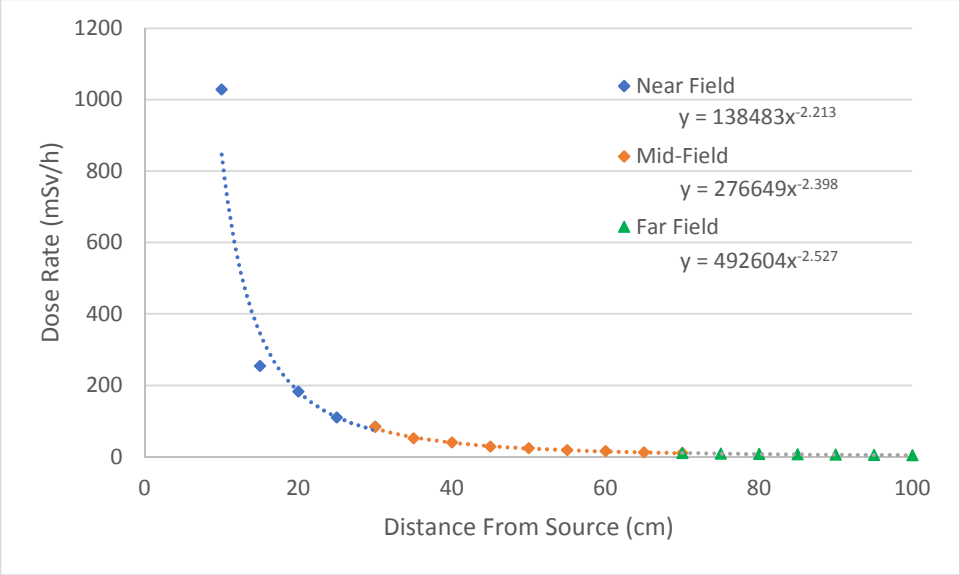

Figure 14. Breakdown of dose rates inside the straight concrete tunnel geometry, segmented into near, mid and far range

The final calculation using the straight tunnel geometry was similar to the first two iterations, but with the tunnel structure made of iron. Iron was selected because the density, $\rho = 7.87$ g/cm^3, is in between concrete and lead densities, and steel (~99% iron) is a common building material. The dose rate inside the iron tunnel dropped off at a rate similar to the lead tunnel above, following the function $r^{-2.30}$. The dose rate in the $-x$ direction, opposite of the tunnel, decreased at a rate very close to the inverse square law following the function $r^{-2.08}$. (Figure 15)

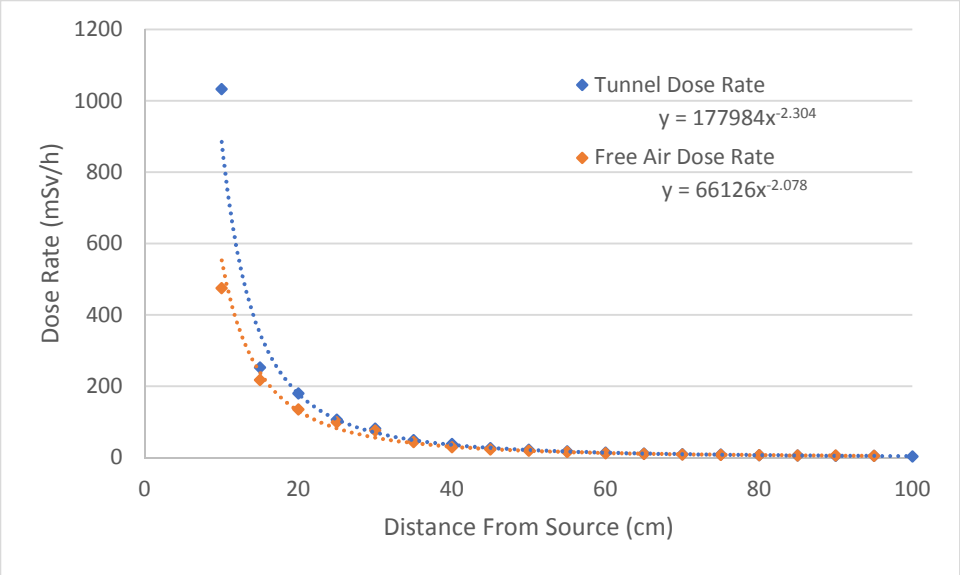

Figure 15. Dose rates both inside and outside (free air) the straight iron tunnel geometry

The data in each of these plots for the three straight tunnel materials investigated can easily be visualized using radiation field heat maps. Using an elemental edit type tally, fluence can be calculated for each tetrahedral cell in the mesh. The fluence across the geometry can then be visualized using Tecplot360®. The three images in Figure 16 depict the three tunnel materials used in the MCNP® calculations. The images are overhead views of a slice in the Y-plane, intersecting the point source. The blue areas in the heat maps represent the lowest dose rate while the white area depicts the highest dose rate immediately surrounding the point source.

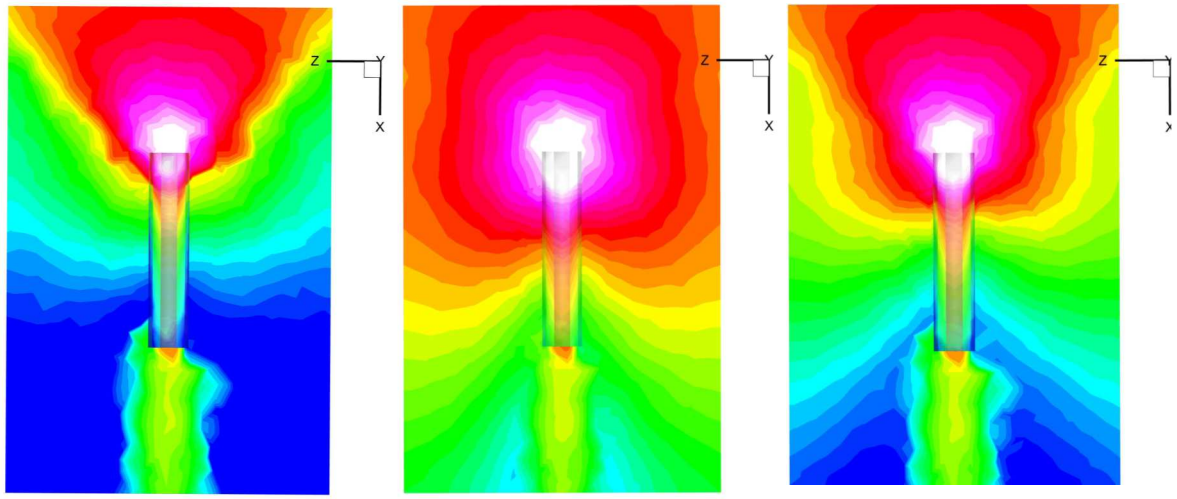

Figure 16. Overhead radiation fields of the three different straight tunnel materials, lead (left), concrete (center) and iron (right)

The T-intersection tunnel design was run two times; the first iteration with a tunnel made of lead, and the second with a tunnel made of concrete. All of the radiation dose rate measurements in the 'T' crossing tunnel were made out of line-of-site of the Cs-137 source, which was positioned at the far end of the narrow tunnel. Down the crossing tunnel, measurements were taken along both the near and far walls. Figure 17 is a comparison of the results for the near wall versus the far wall at 2 cm off each wall. The functional dependency on distance from the tunnel intersection is provided in the plot. For the near wall, the relationship between dose rate and distance followed $r^{-3.20}$ while the far wall followed $r^{-3.09}$. At 5 cm from the intersection, the near wall dose rate was 65% higher than the far wall; however, at 25 cm from the intersection, the near wall dose rate was 77% lower than the far wall.

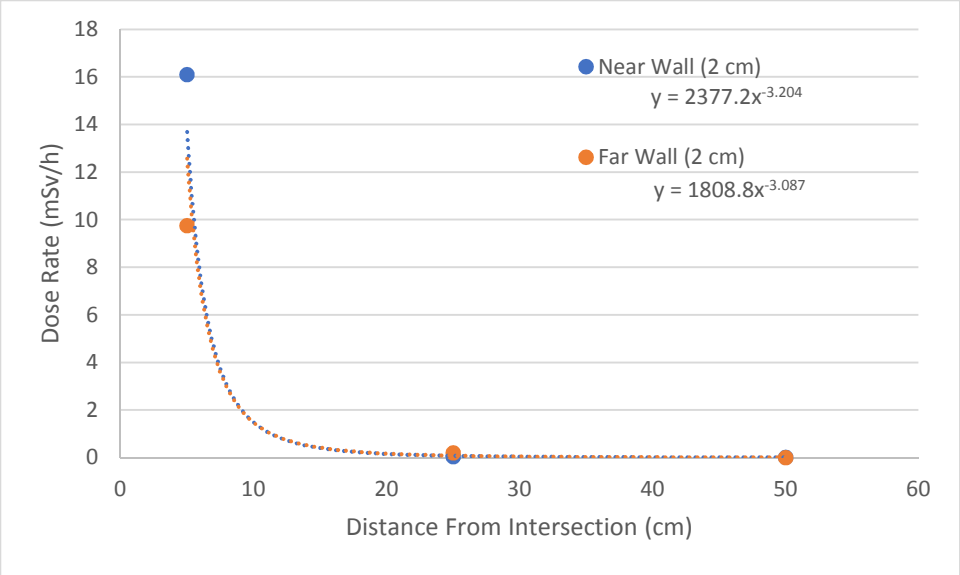

Figure 17. Dose rates along both the near and far walls inside the lead intersecting tunnel

The values obtained by MCNP® differed from the measurements recorded in the T-intersection tunnel constructed with lead blocks. Figure 18 shows an overhead diagram of the experimental set up and the locations where measurements were taken.

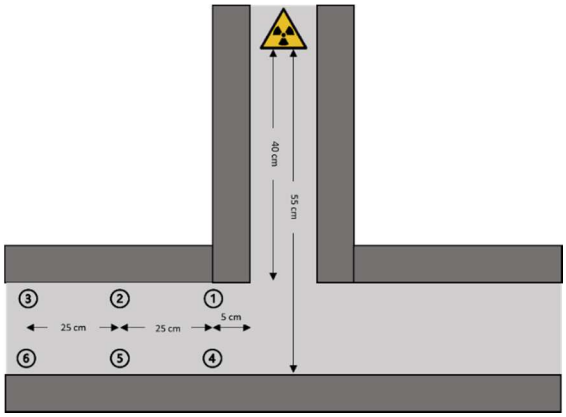

Figure 18. Diagram of the T-intersection geometry with dose rate measurement positions labeled

The results of those measurements and the MCNP® calculated dose rates at the same locations are included in Table 3. The dose rates in the benchmark measurements were related to distance from the intersection by $r^{-1.96}$ for the near wall and $r^{-2.1}$ for the far

wall. The MCNP® calculation provided a much higher dose rate than the physical measurements for both sides of the crossing tunnel for all three distances from the intersection.

Table 3. Dose rates from benchmark measurements and MCNP® calculation for lead T-intersection tunnel configuration

Distance From Intersection (cm)	*Near Wall Positions*	*Benchmark (mSv/h)*	*MCNP (mSv/h)*	*Far Wall Positions*	*Benchmark (mSv/h)*	*MCNP (mSv/h)*
5	1	0.227	16.093	4	0.427	9.746
25	2	0.014	0.046	5	0.022	0.204
50	3	0.002	0.012	6	0.003	0.006

The second iteration of the T-intersection calculation included a concrete wall structure. Concrete structures were added to the outside space between the source and the crossing tunnel to minimize transmission through the tunnel structure since concrete is less attenuating. The dose rates down the near and far walls of the crossing concrete tunnel were initially (at 5 cm) smaller than those recorded for the lead tunnel. With increasing distance from the intersection, the dose rates along the near and far walls decreased more slowly than in the lead tunnel. For the near wall at 2 cm off the wall, the relationship between dose rate and distance followed $r^{-0.83}$ and for the far wall it followed $r^{-0.75}$. For the concrete set up, the near wall displayed higher dose rates than the far wall for all distances. (Figure 19)

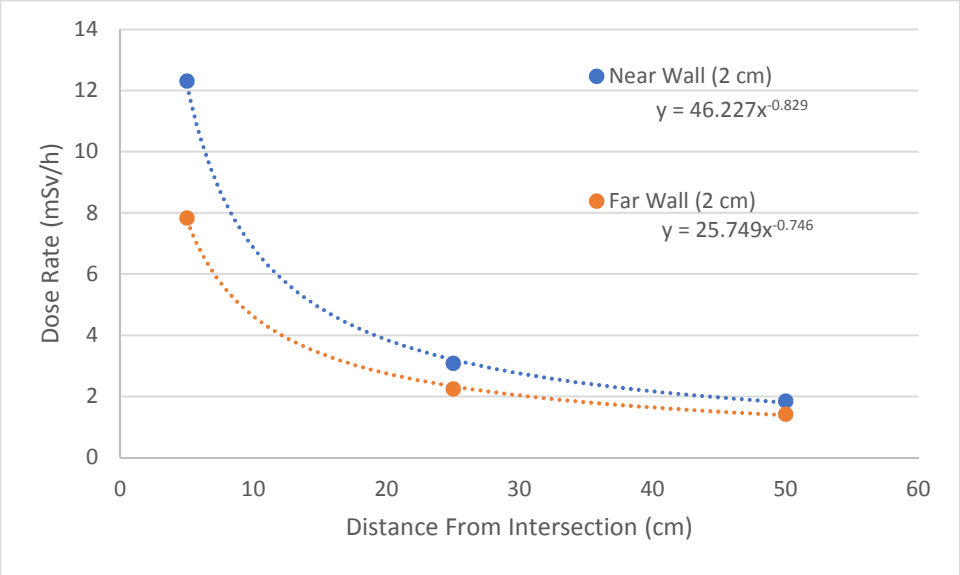

Figure 19. MCNP® calculated dose rates along the near and far walls of the concrete tunnel geometry

The results of the two T-intersection tunnels are visualized in Figure 20 where blue, or green in the concrete tunnel image, represents the lowest dose rate and white represents the highest dose rate. In the heat map for the concrete structure, it can be seen that the dose rates along the near wall are higher than the dose rates along the far wall of the crossing tunnel. The difference between the near and far wall is less discernable in the lead tunnel heat map.

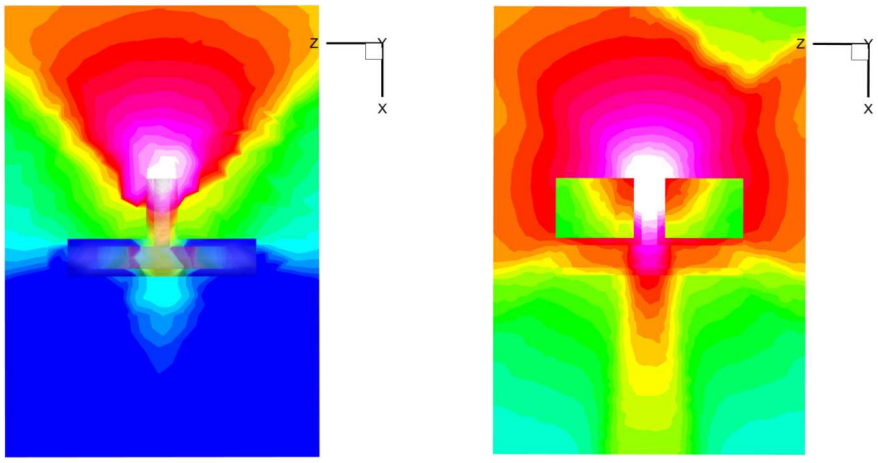

Figure 20. Overhead heat maps of the lead tunnel (left) and concrete tunnel (right) using same color scale

The final small-scale geometry reproduced using Attila® and MCNP® was the curved tunnel. Measurements along the pathlength of the curve reveal that the dose rate inside the curved tunnel can be higher than would be expected when beyond the line-of-sight of the direct beam, but lower than in a free air scenario. At a pathlength of approximately 100 cm, the dose rate in the curved tunnel was 0.094 mSv/h. Further along the tunnel at approximately 125 cm path length, the dose rate was 0.012 mSv/h. These values are much smaller than the free air measurement at 1 meter; however, the heat map (Figure 21) visually shows how scatter inside the tunnel contributes to a higher dose rate than would be expected from transmission through the lead wall. The heat map also shows that the outside curved wall experiences many more photon interactions than the inside wall at the same pathlength. When compared to the benchmark measurements, the MCNP® calculation again provides a higher dose rate. The physical measurement at a pathlength of 100 cm is just 0.032 mSv/h, or about 1/3 of the calculated value in MCNP®. Data from the curved tunnel are included in Appendix C.

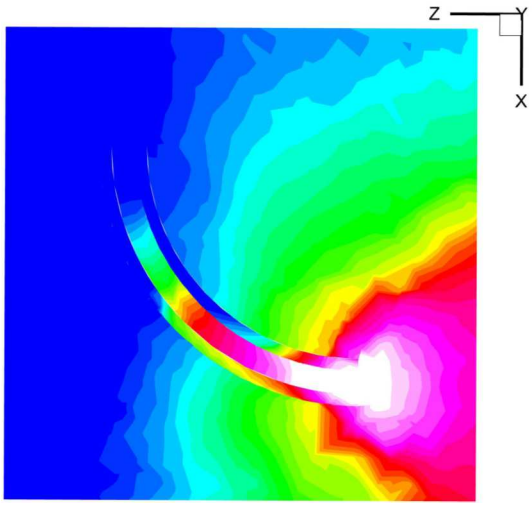

Figure 21. Overhead heat map of the curved tunnel calculation using MCNP

MCNP® Models of Zentrum am Berg Facility Results

After the calculations were validated and completed for small scale geometries, radiological exposure device threat scenarios were modeled using the ZAB facility. The first calculation using the ZAB road tunnel geometry included a Cs-137 source placed in one of the pedestrian walkways connecting two full sized road tunnels. The source activity was scaled to 100 Ci (3.7 TBq) and dose rates were recorded for several positions inside the tunnel. Figure 22 is an overhead view of the tunnels with the gamma radiation field from the Cs-137 source visible along with markers representing the locations of the measurements taken across the width of one of the road tunnels.

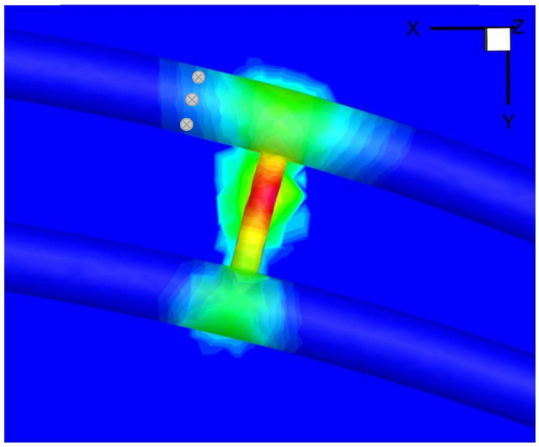

Figure 22. Overhead view of the ZAB road tunnels with a Cs-137 source placed in the connecting pedestrian walkway

Dose rate measurements were recorded for three positions across the width of the road tunnel at a point approximately 10 m from the intersection with the pedestrian tunnel. The measurement closest to the far wall had the highest dose rate, 39.3 μSv/h, while the measurement closest to the near wall had the lowest dose rate, 23.0 μSv/h. Measurements taken closer to the source, inside the narrow pedestrian pathway, produced a distance relationship of $r^{-1.57}$.

The second calculation using the ZAB geometry was created using a Co-60 source placed in the same pedestrian walkway. The same materials, limestone and air, were used in this set up, and measurements were taken in similar locations for comparison. Figure 23 shows a radiation heat map of the Co-60 threat scenario, with the geometry of the tunnel visible. The dose rates across the width of the road tunnel at 10 meters from the intersection ranged from 55.8 μSv/h at the near wall to 99.3 μSv/h at the far wall. In the vicinity of the source inside the narrow pedestrian tunnel, the dose rate was related to distance by $r^{-1.59}$.

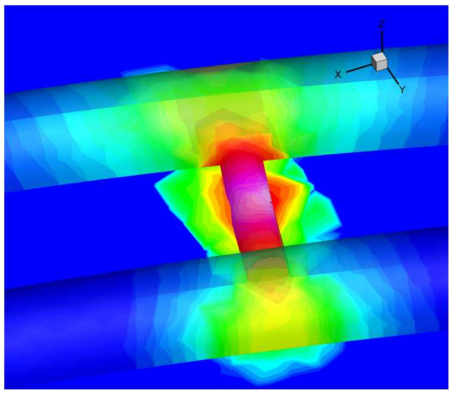

Figure 23. Radiation heat map depicting a Co-60 source positioned in a narrow connecting passageway in the ZAB

DISCUSSION

MCNP® Models of the Benchmark Measurement Geometries

The first calculation completed was the free air measurement using Cs-137 source with activity, A = 28.3 GBq. This configuration was designed to validate that the source spectrum, cross sections, and dose response functions were all appropriately created within the Attila® project and MCNP® calculation. The results show excellent agreement with accepted gamma ray constants for Cs-137. The calculated value of 3.01 mSv/h was 1% less than the predicted value of 3.04 mSv/h for the Cs-137 source simulating the source used in the benchmark measurements. The calculated dose rate had an uncertainty of 0.35% at 1σ and the tally results passed 10/10 statistical tests run in MCNP®. This agreement was the driving factor for selecting the H*(10) dose conversion coefficients in ICRU 57 rather than the kerma conversion coefficients provided in ICRU 57 Table A.1. The kerma conversion coefficients over-valued the low energy photon contribution, which would not penetrate deep enough into tissue to be considered for deep dose. For example, the ratio of H*(10) to kerma for 20 keV photons is 0.61, and decreases as the photon energy approaches 10 keV. In high scatter environments, there are many low energy photons generated via Compton scattering or X-ray fluorescence. The agreement between the calculated and accepted values provided confidence in the subsequent Attila® projects and MCNP® calculations.

The small scale, straight tunnel configuration provided a simple geometry designed to investigate scatter and streaming affects. The first straight tunnel calculation in MCNP® included a lead tunnel structure, representing the highest atomic number of the materials

used in the calculations and simulating the benchmark measurements taken using a handheld detector. The benchmark measurement data included dose rates at 25, 50 and 100 cm from the Cs-137 source and yielded a functional dependency on distance of $r^{-2.39}$. This was a slightly stronger relationship than was calculated using the fluence through the unstructured mesh in MCNP®, meaning the dose rate dropped off more quickly as a function of distance. The MCNP® calculated dose rate to distance relationship was $r^{-2.31}$ from 10 cm to 100 cm down the length of the tunnel. Despite exhibiting a similar relationship with distance, the physical measurements were significantly lower than the MCNP® calculated measurements. At 50 cm, the benchmark measurement recorded was 12.28 mSv/h, which is 36% lower than the MCNP® calculate value, 19.30 mSv/h at the same distance. The difference between the two values is greater than the 20% tolerance afforded by the manufacturer for the handheld Radeye detector. It is important to note that the Radeye detector manual states that the detector is not sensitive to photons below 60 keV; therefore, it is likely that much of the low energy fluorescence was not detected in the benchmark study. Additional investigation of the Radeye detector along with MCNP® calculations with appropriate energy cutoff would be required to fully characterize the performance of the instrument.

The inverse square law implies an exponent equal to -2, which means that in a free field, the radiation dose rate drops off more slowly as a function of distance than was observed in the small-scale tunnel. The dose rate inside the well shielded tunnel drops off very quickly as the high scatter angle photons greatly increase dose rate near the source but are not directed down the length of the tunnel. Lead is a high atomic number element with high electron density; therefore, the likelihood of interaction via photoelectric

absorption or Compton scattering is relatively high. The Klein-Nishina formula (equation 3) predicts that the scattering angle of photons would tend towards the direction of travel at 0.662 MeV. The higher probability of interaction along with preferential scatter in the forward direction could explain why the dose rate at 100 cm in the lead tunnel is greater than the dose rate at 100 cm in free air.

The probability of interaction contributes to the increased dose rate at 100 cm, but this same phenomenon also means greater absorption of photons. The probability of Compton scattering is dependent on the energy of the photon, decreasing with increasing photon energy. This means that the mean free path of a photon entering the lead wall is greater than the mean free path of a photon after it interacts in the lead wall; therefore, photons scattering in the lead wall must pass through more relaxation lengths to exit the lead than it took to enter it. The difference in self-absorption can be seen when analyzing the iron and concrete tunnels. The iron tunnel, with a density of 7.87 g/cm^3, produced higher dose rates at 100 cm than in the lead tunnel or free air. The lead tunnel created a higher dose rate at 100 cm than the free air measurement, implying that there is an optimization between the probability of scattering and the impact of self-absorption. The iron tunnel had the highest dose rate recorded near the source at the 10 cm position of the three different materials used. Self-absorption in the tunnel walls is hypothesized to be why the iron tunnel does not create the most significant streaming effect of the materials used, despite having the highest initial dose rate.

The final iteration, containing a concrete tunnel structure, yielded the highest dose rates of the three materials used at all positions except the 10 cm position in the iron tunnel. Concrete is much denser than air with many more electrons available for

interaction, yet it is not so dense as to completely attenuate photons traveling through the wall thickness. Of the three materials used in the MCNP® calculations, the concrete tunnel exhibits the most evidence of streaming as the dose rates within the tunnel are the largest observed and significantly larger than the free air calculations.

The T-intersection scenario provided initially confounding data for radiation dose rates along the walls of the crossing tunnel. The first calculation using the T-intersection consisted of lead wall material to mimic the benchmark study; however, the results were not as hypothesized. In the benchmark study, the dose rates along the near wall consistently measured lower than those along the far wall. Also, the physical measurements displayed a functional dependence on distance from the intersection very near the inverse square law. In the MCNP® calculation of the same tunnel, the dose rates along the near wall were initially higher at the 5 cm position but gradually became lower than the far wall dose rates by the 25 cm position. The increased dose rate at the 5 cm distance from the intersection along the near wall could be caused by an area of favorable scattering angles emitting from the primary beam stop segment on the far wall. Using equation 4, a 0.662 MeV photon scattering 180° would retain only 0.184 MeV of energy and would be more likely to deposit energy nearby along the scattered path. At 25 cm, the dose rate along the near wall becomes lower than the dose rate along the far wall. This could be representative of the benchmark study measurements with the short, 5 cm, distance succumbing to a small area of favorable scattering that was not observed in the benchmark.

The concrete T-intersection tunnel results were not consistent with the lead T-intersection tunnel results. The functional dependence on distance had a much smaller

order of magnitude along the crossing tunnel length than observed in the lead tunnel; on the order of r^{-1} versus r^{-3}. The lower order dependence could be the result of increased scatter escape within the walls along with skyshine from above or below the geometry in the third dimension.

The curved tunnel segment provided an interesting look at the potential of radiation streaming. The dose rates inside of the curved tunnel were lower than expected at equivalent distances in free air, but they were also greater than what is expected to transmit through the thickness of absorber. The curved tunnel results can be observed in the heat map provided in Figure 21 and supports the data analyzed from the straight tunnel geometry. The smaller dose rates observed in the physical measurements could again be related to the sensitivity of the instrument used. If the dose rate is almost entirely due to radiation scatter, then the average energy of photons would be far less than the 0.662 MeV emission, and less than the maximum backscatter photon of 0.184 MeV. As scattered photon energies dip below the 60 keV threshold indicated by the manufacturer, the low energy photons may not be detected and may not contribute to the dose recorded. As with the initial analysis of the performance of the Radeye detector, additional investigation would be required to validate that the observed differences were a product of low energy contribution.

MCNP® Models of the Zentrum am Berg Facility

The ZAB calculations were designed to take the step from a proof of concept to initial full scale implementation. The first scenario included a 100 Ci Cs-137 source placed in a crossing pedestrian tunnel between two full sized road tunnels. The amount of shielding surrounding the tunnels ensured that virtually no transmission of the primary beam was

possible through the thickness of the absorbing limestone to the measurement points in the road tunnel. The overhead heat map confirmed what was observed in the measurements across the width of the large road tunnel. The dose rates were lower along the near wall of the road tunnel, increasing across the width of the tunnel to the far wall. This phenomenon was consistent at increased distance from the source along the road tunnel, unlike the small scale T-intersection tunnel made of lead. The ZAB road tunnel had a slight curve which likely impacted the scattering of the beam and prevented the radiation hot spot observed on the near wall in the small scale model. Inside the pedestrian walkway, the radiation field did not follow the functional dependence on distance predicted by the small scale straight tunnel. The larger volume of the pedestrian tunnel yielded a relationship with distance of $r^{-1.57}$ and a dose rate of 446.8 mSv/h at 1 meter. Dose rate has a linear relationship with activity; therefore the 1 meter dose rate measurement in the ZAB tunnel can be compared to the 1 meter dose rate in the small scale straight tunnel modeled. When scaling for activity, the ZAB dose rate at 1 meter was smaller than the dose rate at 1 meter from any of the three straight tunnel calculations completed. This implies that the impact of scattering increases as tunnels become narrower. The scaled dose rate at 1 meter in the ZAB was still greater than was calculated in free air as expected, with additional contributions from scatter in the tunnel walls.

The final calculation of the ZAB geometry included a 100 Ci Co-60 source in the same pedestrian walkway. Co-60 emits two gamma rays (1.17 and 1.33 MeV), both at higher energies than Cs-137 (0.662 MeV), resulting in a gamma ray constant of greater magnitude. Also, the gamma ray emission energies of Co-60 are sufficient to interact via pair production (>1.02 MeV), introducing a new radiation transport element to the

calculation. The results of the Co-60 threat scenario were similar to the results presented in the Cs-137 scenario. The radiation field in the wider ZAB road tunnel had a very similar distribution; however, the dose rates from the Co-60 source were much larger. The dose rate at the mid-point of the road tunnel width approximately 10 meters from the intersection of the narrow pedestrian tunnel was 84.5 μSv/h, which is 146% larger than at the same position in the Cs-137 set up. Despite the higher dose rates, the Co-60 calculation demonstrated again that the near wall in the road tunnel consistently had lower dose rates than the far wall. The near-source measurements in the pedestrian tunnel yielded a very similar functional dependence on distance, $r^{-1.59}$, with a dose rate of 1394.6 mSv/h at 1 meter. Figure 24 compares the two threat scenarios using radiation heat maps of the same color scale to show the similarities in the radiation fields and the behavior of the dose rates at increased distances from the source within the ZAB the road tunnel.

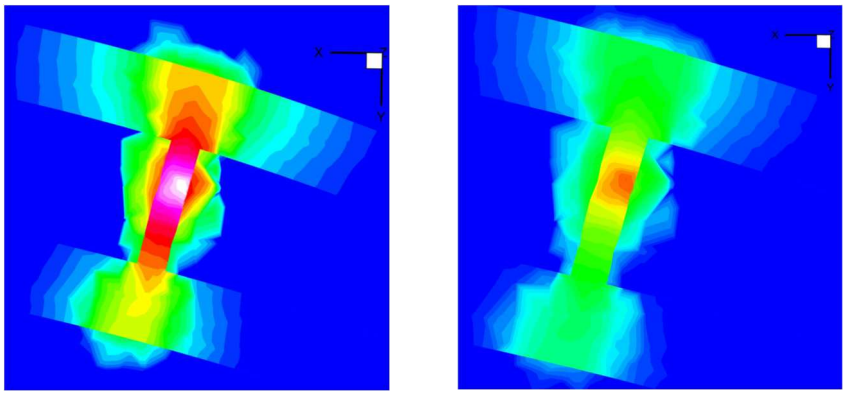

Figure 24. Overhead view of radiation fields inside the ZAB tunnels emanating from Co-60 (left) and Cs-137 (right)

Radiation field images convey information useful to operators responding to an emergency. The data gathered in this study support that the radiation dose rates observed in MCNP® modeling visualizations are representative of expected dose rates. Radiation fields in high scattering environments such as the ZAB tunnel cause radiation

dose rates to be higher in both the near and far field than would be predicted by the inverse square law, providing evidence of radiation streaming. At crossing intersections, like the T-intersection or the ZAB roadway exhibited, a combination of skyshine and scattering of the primary beam on the far wall of the intersection both appear to contribute to higher dose rates than expected from only transmission through the surrounding material. The visual aids created using information from radiation transport code data can be used by emergency planners or incident commanders to support decision making. Future projects could take advantage of the benefits provided by the software used in this study to develop tools for real time use modeling of CBRN environments.

CONCLUSION

This project evolved from benchmark measurements of a Cs-137 source in several shielded configurations to calculating dose rates in complex subsurface structures via a radiation transport code. The initial benchmark measurements supported the hypothesis that radiation scattering in well shielded and confined environments would complicate the radiation field and result in measurable dose rates beyond the line-of-sight of the radiation source. The subsequent MCNP® calculations were supported by the benchmark study, validating the accuracy of the computational models, and further demonstrating that the hypothesis was correct. The data show that dose rates in the well shielded configurations were higher than in free air, and the radiation field could not be characterized by the inverse square law; therefore, the data provide evidence of radiation streaming within the well shielded tunnels modeled.

The free air MCNP® model exhibited agreement with the accepted gamma ray constant for Cs-137 within 1% with a 1σ uncertainty of 0.35%. The straight tunnel configurations confirmed the hypothesis that radiation scatter inside well shielded and narrow spaces causes dose rates to be higher than at equivalent distances in a free field. The dose rate at 100 cm from the source was 18.2% greater in the lead tunnel (3.56 mSv/h) than in the free field (3.01 mSv/h). In all of the straight tunnel models, the functional dependency on distance from the source resulted in higher dose rates than predicted by the inverse square law, ranging from $r^{-2.29}$ in the concrete tunnel to $r^{-2.31}$ in the lead tunnel. Of the three materials used in the straight tunnel models, concrete yielded the highest dose rates at increased distances from the source within the tunnel and lead

yielded the lowest relative dose rates. This implies that there is an optimization between the probability of scattering and self-absorption in the tunnel materials. The T-intersection model results quantified scatter at distances from a perpendicular crossing tunnel. The dose rates along the near wall of the crossing tunnel exhibited a radiation hot spot near the intersection that was likely caused by a combination of skyshine and favorable scattering angles off the segment of wall exposed to the primary beam. The dose rates along the near wall decreased with distance from the intersection, becoming lower than the dose rates along the far wall at 25 cm. The curved tunnel model created a useful visualization of the effects of scatter in narrow passageways, and the radiation streaming can be seen beyond the line-of-sight of the source in Figure 21. The final part of this project was implementing the modeling techniques into real world threat scenarios for subterranean infrastructure. Two models of a full sized underground roadway (ZAB) were completed using two known radiological exposure device threat materials, Cs-137 and Co-60. Both models resulted in similarly shaped radiation fields, but Co-60 yielded much higher dose rates from the same source activity. The dose rates across the width of the crossing road tunnel at a point 10 meters from the intersection of the pedestrian walkway confirmed that the near wall offered lower radiation dose rates than the far wall upon approach. The radiation field visualization of the two threat scenarios shown in Figure 24 supports that the near wall offers more protection during egress or ingress than the far wall down the length of the tunnel. These findings could prove useful to decision makers facing a subsurface infrastructure CBRN incident and could lead to the development of tools that can be implemented into emergency preparedness framework.

REFERENCES

Agricola, G., Hoover, H., & Hoover, L. H. (2014). *De Re Metallica*. Martino Publishing.

AlpTransit. (2010, April 22). *Project data – Raw Construction Gotthard Base Tunnel - 57 km*. Gotthard Base Tunnel. Retrieved May 25, 2022, from http://www.57km.ch/fileadmin/gotthard/Downloads/Dokumente_PDF_e/Project_data_Gotthard_raw_construction_e.pdf

Blackett, Patrick Maynard Stuart, Occhialini, Giuseppe Paolo Stanislao (1933). *Some Photographs of the Tracks of Penetrating Radiation*. Proceedings of the Royal Society of London, Series A, Containing Papers of a Mathematical and Physical Character. 139.839: 699-726

Bland, J., Potter, C., & Homann, S. (2018). (rep.). *Radiological Exposure Devices (RED) Technical Basis for Threat Profile*. Albuquerque, NM: Sandia National Laboratories.

Bogan, J., Feeney, A. (2020, February 17). *Future Cities – Trends and Implications* UK Ministry of Defense. Retrieved April 16, 2022, from https://assets.publishing.service.gov.uk/government/uploads/system/uploads/attachment_data/file/875528/Dstl_Future_Cities_Trends___Implications_OFFICIAL.pdf

Choppin, G., Liljenzin, J.-O., Rydberg, J., & Ekberg, C. (2014). *Radiochemistry and nuclear chemistry* (4th ed.). Elsevier.

Compton, Arthur H., (1923). *A Quantum Theory of the Scattering of X-rays by Light Elements*. Phys. Rev Vol. 21, No. 5: 483-502

Department of Defense. (2018). *Operations in Chemical, Biological, Radiological, and Nuclear Environments*. Joint Publication (JP) 3-11, DOD.

Detwiler, R.S., McConn, R.J., Grimes, T.F., Upton, S.A., Engel, E.J. (2021). *Compendium of Material Composition Data for Radiation Transport Modeling*. Richland, WA; Pacific Northwest National Laboratory.

Einstein, A., (1905a). Über einen die Erzeugung und Verwandlung des Lichtes betreffenden heuristischen Gesichtspunkt. Annalen der Physik 4.

Einstein, A., (1905b). Ist die Trägheit eines Körpers von seinem Energieinhalt abhängig?. Annalen der Physik 18: 639-641.

Federal Bureau of Investigation (FBI). (2016, May 17). Amerithrax or Anthrax Investigation. Retrieved June 5, 2022, from https://www.fbi.gov/history/famous-cases/amerithrax-or-anthrax-investigation

Fischer, M., & Pelzer, R. (2015). *Die Logik des Anschlags*. Campus Publisher.

Hall, E. J., & Giaccia, A. J. (2019). *Radiobiology for the radiologist*. Wolters Kluwer.

Hofer, P. (2019). Coping with Complexity: The Development of Comprehensive Subsurface Training Standards from a Military Perspective. *Berg- Und Hüttenmännische Monatshefte*, 479–504.

International Atomic Energy Agency (2006). (rep.). *Dangerous Quantities of Radioactive Material (D-Values)* (Ser. Emergency Preparedness and Response). Vienna, AT: IAEA.

International Commission of Radiological Protection (2007). *The 2007 Recommendations for the System of Radiological Protection*. ICRP Publication 103. Ann. ICRP 37 (2-4)

International Commission of Radiological Protection (1977). *Recommendations of the ICRP*. ICRP Publication 26. Ann. ICRP 1 (3)

International Commission on Radiation Units and Measurements (1998). (rep.). *Conversion Coefficients for use in Radiological Protection Against External Radiation*. ICRU Report 57: ICRU

Johnson, T. E. (2017). *Introduction to Health Physics* (5th ed.). McGraw-Hill.

Knoll, G. F. (2010). *Radiation Detection and Measurement* (4th ed.). Hoboken, NJ: Wiley.

Livingston, B., Costeira, T., Arguello, D., Cuellar, J., & Falo, G. (2020). *Tech Guide 238: Radiological Sources of Potential Exposure and/or Contamination*. US Army Public Health Center.

Los Alamos National Laboratory (2008). *MCNP User Manual, Version 5. Los Alamos, NM; LANL*.

Mann JE, Zoeger N, Koppitsch R, Brandl A. (2018). *Investigation of Dose Rates Exterior to an Above-Ground Waste Storage Facility Using Radiation Transport Models*. Health Phys. 2018 Oct; 115(4):539-544

McPherson, M. J. (2009). *Subsurface Ventilation Engineering*. Mine Ventilation Services, Inc.

Metropolis, N. (1987). *The Beginning of the Monte Carlo Method*. Los Alamos Science, Special Edition.

Owen, R. (2016). *The Litvinenko Inquiry: Report into the Death of Alexander Litvinenko*. Stationery Office.

Parker, A., Brandl, A., Hofer, P., & Galler, R. (2021). Doses and Dose Rates from CBRN Attacks in Subterranean Environments. *DCNA Disaster Research Days*.

Smithson, Amy E., (2000) Rethinking the Lessons of Tokyo, Ataxia: The Chemical and Biological Terrorism Threat and the US Response. Washington, DC; The Henry L. Stimson Center.

Unger, L., & Trubey, D. K., (1981) Specific Gamma-Ray Dose Constants for Nuclides Important to Dosimetry and Radiological Assessment. Oak Ridge, TN; Oak Ridge National Laboratory.

VisitNorway. *Lærdalstunnelen - Worlds Longest Road Tunnel*. Norway. (2022, May). Retrieved June 1, 2022, from https://www.visitnorway.com/listings/l%C3%A6rdalstunnelen-worlds-longest-road-tunnel/12205/

APPENDIX A

Table D.1. Select conversion coefficients from ICRU 57 Table A.21 for the dose equivalent, H*(10) for photon fluence in free air

Photon Energy (MeV)	H*(10)/K (Sv/Gy)	H*(10)/φ (pSv cm^2)
0.01	0.008	0.061
0.015	0.26	0.83
0.02	0.61	1.05
0.03	1.1	0.81
0.04	1.47	0.64
0.05	1.67	0.55
0.06	1.74	0.51
0.08	1.72	0.53
0.1	1.65	0.61
0.15	1.49	0.89
0.2	1.4	1.2
0.3	1.31	1.8
0.4	1.26	2.38
0.5	1.23	2.93
0.6	1.21	3.44
0.8	1.19	4.38
1	1.17	5.2
1.5	1.15	6.9
2	1.14	8.6
3	1.13	11.1
4	1.12	13.4
5	1.11	15.5
6	1.11	17.6
8	1.11	21.6
10	1.1	25.6

APPENDIX B

Example output file from MCNP® (free air calculation)

```
         Code Name & Version = MCNP_6.20, 6.2.0

     _/      _/        _/_/_/       _/      _/       _/_/_/          _/_/_/
    _/_/  _/_/      _/             _/_/    _/       _/    _/      _/
   _/  _/  _/      _/             _/  _/  _/       _/_/_/        _/_/_/
  _/      _/      _/             _/    _/_/       _/             _/    _/
 _/      _/        _/_/_/       _/      _/       _/              _/_/

  +------------------------------------------------------------------------+
  | Copyright (2018).  Los Alamos National Security, LLC.  All rights     !
  | reserved.                                                              !
  |  This material was produced under U.S. Government contract             !
  | DE-AC52-06NA25396 for Los Alamos National Laboratory, which is         !
  | operated by Los Alamos National Security, LLC for the U.S.             !
  | Department of Energy. The Government is granted for itself and         !
  | others acting on its behalf a paid-up, nonexclusive, irrevocable       !
  | worldwide license in this material to reproduce, prepare derivative    !
  | works, and perform publicly and display publicly. Beginning five (5)   !
  | years after February 14, 2018, subject to additional five-year         !
  | worldwide renewals, the Government is granted for itself and others    !
  | acting on its behalf a paid-up, nonexclusive, irrevocable worldwide    !
  | license in this material to reproduce, prepare derivative works,       !
  | distribute copies to the public, perform publicly and display          !
  | publicly, and to permit others to do so. NEITHER THE UNITED STATES     !
  | NOR THE UNITED STATES DEPARTMENT OF ENERGY, NOR LOS ALAMOS NATIONAL    !
  | SECURITY, LLC, NOR ANY OF THEIR EMPLOYEES, MAKES ANY WARRANTY,         !
  | EXPRESS OR IMPLIED, OR ASSUMES ANY LEGAL LIABILITY OR RESPONSIBILITY   !
  | FOR THE ACCURACY, COMPLETENESS, OR USEFULNESS OF ANY INFORMATION,      !
  | APPARATUS, PRODUCT, OR PROCESS DISCLOSED, OR REPRESENTS THAT ITS USE   !
  | WOULD NOT INFRINGE PRIVATELY OWNED RIGHTS.                            !
  +------------------------------------------------------------------------+

1mcnp     version 6.mpi ld=07/01/21                    06/04/22 09:24:05
 ***********************************************************************                probid =  06/04/22 09:24:05
 i=freeair1.mcnp.i

  comment.  Physics models disabled.
         1-       freeair1
         2-       c
         3-       c Attila calculation "FreeAir1"
         4-       c
         5-       c -------------------------- Input Information ------------------------------ 80
         6-       c Attila GUI created MCNP6 Input
         7-       c Attila Version (not available)
         8-       c Input File Creation Date: Fri Jun 3 12:30:11 2022
         9-       c RxMesher version          : 1.0.0
        10-       c Simmetrix MeshSim version : 14.0-200321
        11-       c Global mesh size          : 0.2 m
        12-       c Generated                 : 2022-06-03T11:42:14-06:00
        13-       c Solid Geometry :
        14-       c   Filename     : FreeAirBox.x_t
        15-       c   Last changed : 2022-06-03T11:12:20-06:00
        16-       c   MD5 checksum : 338468b012d96151d4fd1e00bccac3b0
        17-       c Note: RTT Mesh has added cell flags for MCNP Abaqus part and pseudo-cell.
        18-       c Associated Abaqus Unstructured Mesh :
        19-       c   Filename     : freeairbox.abaq
        20-       c   Generated    : 2022-06-03T12:30:11
        21-       c   MD5 checksum : 058be605f3067f2a0518fbf868030ea8
        22-       c n_points = 33911
        23-       c n_sides  = 10406
        24-       c n_cells  = 163271
        25-       c Mesh Bounding Box (cm):
        26-       c  x: -250.000 -  250.000
        27-       c  y: -250.000 -  250.000
        28-       c  z: -250.000 -  250.000
        29-       c
        30-       c Number of Attila Regions                : 3
        31-       c Number of Abaqus Parts/MCNP Pseudo-Cells : 3
        32-       c Number of Materials                     : 1
        33-       c
        34-       c  Mesh Region/Pseudo-Cell Information
        35-       c   Attila Region #    : 2
        36-       c   Attila Region Name : "Source"
        37-       c   Abaqus Part #      : 1
        38-       c   Abaqus Part Name   : "Source"
        39-       c   MCNP Pseudo-cell # : 1
        40-       c   Material           : "Air_1"
        41-       c    MCNP Material     : m1
        42-       c    Density           : 0.0012 g/cc
        43-       c   Mesh Data
        44-       c     Meshed Volume    : 1 cm**3
        45-       c     # Cells          : 11
        46-       c     % of Total Cells : 0.01%
```

```
c
c   Attila Region #    : 1
c   Attila Region Name : "Air"
c   Abaqus Part #      : 2
c   Abaqus Part Name   : "Air"
c   MCNP Pseudo-cell # : 2
c   Material           : "Air_1"
c    MCNP Material     : m1
c    Density           : 0.0012 g/cc
c   Mesh Data
c     Meshed Volume    : 1.24999e+08 cm**3
c     # Cells          : 163248
c     % of Total Cells : 99.99%
c
c   Attila Region #    : 3
c   Attila Region Name : "Detector"
c   Abaqus Part #      : 3
c   Abaqus Part Name   : "Detector"
c   MCNP Pseudo-cell # : 3
c   Material           : "Air_1"
c    MCNP Material     : m1
c    Density           : 0.0012 g/cc
c   Mesh Data
c     Meshed Volume    : 1000 cm**3
c     # Cells          : 12
c     % of Total Cells : 0.01%
c
c ------------------------ End Input Information ---------------------------- 80
c
c ----------------------------- Cell Cards ---------------------------------- 80
1     1     -0.0012      0                               u=1
2     1     -0.0012      0                               u=1
3     1     -0.0012      0                               u=1
4     0                  0                               u=1 $ background
5     0                  100 -101 102 -103 104 -105   fill=1 $ fill cell
6     0                  (-100:101:-102:103:-104:105)
c --------------------------- End Cell Cards ------------------------------- 80

c ---------------------------- Surface Cards ------------------------------- 80
c
100 px -255
101 px 255
102 py -255
103 py 255
104 pz -255
105 pz 255
c -------------------------- End Surface Cards ------------------------------ 80

c ----------------------------- Data Cards ---------------------------------- 80
c Embedded Geometry Specification
embed1 meshgeo=abaqus mgeoin=freeairbox.abaq
       meeout=freeair1.mcnp.eeout
       filetype=ascii
       background=4
       matcell= 1 1 2 2 3 3
c
c Materials
c
c  Material 1: "Air_1"
c  Constituents (weight %):
c o16-8016 (0.24) n14-7014 (0.76)
m1  8016 -0.24 7014 -0.76
c
c Mode (Only n and/or p Currently Accepted)
mode p
c
c Cell Importances
imp:p 1 1 1 1 1 0
c
c Source Definition
sdef pos=volumer erg=d1 par=p wgt=1
c      Region "Source"
c      Spectrum "Cs137"
si1 L  0.662
sp1 d  1
c
c Histories (or Computer Time Cutoff)
nps 1e8
c ctme 1
c
c
c Tallies or embee cards
fc4  tally "DetectorDose"
f4:p  ( 3 )
c de/df4 user-defined response function "H*10"
de4 log  0.01              0.015             0.02              &
         0.03              0.04              0.05              &
         0.06              0.08              0.1               &
         0.15              0.2               0.3               &
         0.4               0.5               0.6               &
         0.8               1                 1.5               &
         2                 3                 4                 &
         5                 6                 8                 &
         10
df4 log  0.061             0.83              1.05              &
```

```
      142-                0.8100000000000001 0.64               0.55               &
      143-                0.51               0.53               0.61               &
      144-                0.89               1.2                1.8                &
      145-                2.38               2.93               3.44               &
      146-                4.38               5.2                6.9                &
      147-                8.6                11.1               13.4               &
      148-                15.5               17.6               21.6               &
      149-                25.6
      150-       c
      151-       c embee14 tally "RadiationField"
      152-       embee14:p embed=1 errors=yes
      153-       c embde/embdf14 user-defined response function "H*10":
      154-       embde14  0.005             0.01               0.015              &
      155-             0.02               0.03               0.04               &
      156-             0.05               0.06               0.08               &
      157-             0.1                0.15               0.2                &
      158-             0.3                0.4                0.5                &
      159-             0.6                0.8                1                  &
      160-             1.5                2                  3                  &
      161-             4                  5                  6                  &
      162-             8                  10
      163-       embdf14  0                 0.061              0.83               &
      164-             1.05               0.8100000000000001 0.64               &
      165-             0.55               0.51               0.53               &
      166-             0.61               0.89               1.2                &
      167-             1.8                2.38               2.93               &
      168-             3.44               4.38               5.2                &
      169-             6.9                8.6                11.1               &
      170-             13.4               15.5               17.6               &
      171-             21.6               25.6
      172-       c
      173-       c
      174-       c L'Ecuyer 63-bit random number generator (period=9.2E18)
      175-       rand gen=2
      176-       c
      177-       print -85 -86 -87 -98
      178-       c
      179-       c --------------------------- End Data Cards -------------------------------- 80
      180-       c End MCNP Input
****************************************************
* Random Number Generator  =                    2 *
* Random Number Seed       =                    1 *
* Random Number Multiplier =  9219741426499971445 *
* Random Number Adder      =                    1 *
* Random Number Bits Used  =                   63 *
* Random Number Stride     =               152917 *
****************************************************
****************************************
***** ABAQUS Input File Statistics *****
****************************************
      File:           freeairbox.abaq

      Number of Parts                                          3
      Number of Assemblies                                     1
      Number of Instances                                      3
      Number of Materials                                      1

      Number of Parts with 1st Order Tets                      3
      Number of Parts with 1st Order Pents                     0
      Number of Parts with 1st Order Hexs                      0
      Number of Parts with 2nd Order Tets                      0
      Number of Parts with 2nd Order Pents                     0
      Number of Parts with 2nd Order Hexs                      0

                                    UNASSEMBLED Maximums
      Total Number of 1st Order Tets                      163271
      Total Number of 1st Order Pents                          0
      Total Number of 1st Order Hexs                           0
      Total Number of 2nd Order Tets                           0
      Total Number of 2nd Order Pents                          0
      Total Number of 2nd Order Hexs                           0
      Total Number of Elements                            163271
      Total Number of Nodes                                33911
      Max   Number of Pseudo-Cells                             6

                                    PART Maximums
      Maximum Number of Nodes                              33893
      Maximum Number of 1st Order Tets                    163248
      Maximum Number of 1st Order Pents                        0
      Maximum Number of 1st Order Hexs                         0
      Maximum Number of 2nd Order Tets                         0
      Maximum Number of 2nd Order Pents                        0
      Maximum Number of 2nd Order Hexs                         0
      Maximum Number of Elements                          163248
      Maximum Number of Materials                              1
      Maximum Number of Volume Source Sets                     1
      Maximum Number of Statistical Regions                    1
      Maximum Number of Material Elements                 163248
      Maximum Number of Statistical Region Elements       163248

                                    ASSEMBLED Maximums
      Total Number of Pseudo-Cells                             3
      Total Number of Elements                            163271
      Total Number of Nodes                                33911
********************
```

```
***** PART DATA *****
********************
***** PART #   1    source
      Number of 1st Order Tets                 11
      Number of 1st Order Pents                 0
      Number of 1st Order Hexs                  0
      Number of 2nd Order Tets                  0
      Number of 2nd Order Pents                 0
      Number of 2nd Order Hexs                  0
      Number of Nodes                           9
      Number of Materials                       1
      Number of Statistical Regions             1
      Number of Source Sets                    11
      Maximum Number in any Part Set
                Material Elements              11
                Statistical Elements           11
***** PART #   2    air
      Number of 1st Order Tets             163248
      Number of 1st Order Pents                 0
      Number of 1st Order Hexs                  0
      Number of 2nd Order Tets                  0
      Number of 2nd Order Pents                 0
      Number of 2nd Order Hexs                  0
      Number of Nodes                       33893
      Number of Materials                       1
      Number of Statistical Regions             1
      Number of Source Sets                     0
      Maximum Number in any Part Set
                Material Elements           163248
                Statistical Elements        163248
***** PART #   3    detector
      Number of 1st Order Tets                 12
      Number of 1st Order Pents                 0
      Number of 1st Order Hexs                  0
      Number of 2nd Order Tets                  0
      Number of 2nd Order Pents                 0
      Number of 2nd Order Hexs                  0
      Number of Nodes                           9
      Number of Materials                       1
      Number of Statistical Regions             1
      Number of Source Sets                     0
      Maximum Number in any Part Set
                Material Elements              12
                Statistical Elements           12
*************************
***** MATERIAL DATA *****
*************************
***** MATERIAL #   1    air_1
*************************
***** INSTANCE DATA *****
*************************
***** INSTANCE #   1    sourceP1                              sourceP1
***** INSTANCE #   2    airP1                                 airP1
***** INSTANCE #   3    detectorP1                            detectorP1
*****************************************************************************************************************************
*  Building the Global Tracking Model                                                                                       *
*****************************************************************************************************************************
Adding Instance #     1   :  sourceP1                                  [Part:]   sourceP1
       First 1st Order TET  element number:            1      Last  1st Order TET  element number:           11
       First 1st Order PENT element number:            0      Last  1st Order PENT element number:            0
       First 1st Order HEX  element number:            0      Last  1st Order HEX  element number:            0
       First 2nd Order TET  element number:            0      Last  2nd Order TET  element number:            0
       First 2nd Order PENT element number:            0      Last  2nd Order PENT element number:            0
       First 2nd Order HEX  element number:            0      Last  2nd Order HEX  element number:            0
                                                              Last GLOBAL element         :           11
                                                              Last GLOBAL node            :            9
       Translate:      0.000000000000000     0.000000000000000     0.000000000000000
       Rotate   :      0.000000000000000     0.000000000000000     0.000000000000000
                       0.000000000000000     0.000000000000000     0.000000000000000
                       0.000000000000000
Adding Instance #     2   :  airP1                                    [Part:]   airP1
       First 1st Order TET  element number:           12      Last  1st Order TET  element number:       163259
       First 1st Order PENT element number:            0      Last  1st Order PENT element number:            0
       First 1st Order HEX  element number:            0      Last  1st Order HEX  element number:            0
       First 2nd Order TET  element number:            0      Last  2nd Order TET  element number:            0
       First 2nd Order PENT element number:            0      Last  2nd Order PENT element number:            0
       First 2nd Order HEX  element number:            0      Last  2nd Order HEX  element number:            0
                                                              Last GLOBAL element         :       163259
                                                              Last GLOBAL node            :        33902
       Translate:      0.000000000000000     0.000000000000000     0.000000000000000
       Rotate   :      0.000000000000000     0.000000000000000     0.000000000000000
                       0.000000000000000     0.000000000000000     0.000000000000000
                       0.000000000000000
Adding Instance #     3   :  detectorP1                                [Part:]   detectorP1
       First 1st Order TET  element number:       163260      Last  1st Order TET  element number:       163271
       First 1st Order PENT element number:            0      Last  1st Order PENT element number:            0
       First 1st Order HEX  element number:            0      Last  1st Order HEX  element number:            0
       First 2nd Order TET  element number:            0      Last  2nd Order TET  element number:            0
       First 2nd Order PENT element number:            0      Last  2nd Order PENT element number:            0
       First 2nd Order HEX  element number:            0      Last  2nd Order HEX  element number:            0
                                                              Last GLOBAL element         :       163271
                                                              Last GLOBAL node            :        33911
       Translate:      0.000000000000000     0.000000000000000     0.000000000000000
       Rotate   :      0.000000000000000     0.000000000000000     0.000000000000000
                       0.000000000000000     0.000000000000000     0.000000000000000
```

```
                      0.000000000000000
    Global Model Extents
    Min X: -2.50000E+02   Max X:  2.50000E+02
    Min Y: -2.50000E+02   Max Y:  2.50000E+02
    Min Z: -2.50000E+02   Max Z:  2.50000E+02
 ************************************************************************************************************************
  * Pseudo-Cell Cross Reference Table                                                                                     *
  ************************************************************************************************************************
  Pseudo-Cell #    MCNP6 Cell #    Instance #    Part #    Material #    Material Name
  -------------    ------------    ----------    ------    ----------    -------------
              1               1             1         1             1    air_1
              2               2             2         2             1    air_1
              3               3             3         3             1    air_1
 ************************************************************************************************************************
 * Global Tracking Model Complete                                                                                        *
 ************************************************************************************************************************
 ***** Estimated Memory Usage for Temporary Mesh Arrays *****
                                    Bytes            MB
      Character Arrays :               1536             0
      Integer Arrays   :           97954052            97
      Real Arrays      :            2440536             2
      Total            :          100396124           100
 ***** Estimated Memory Usage for Permanent Mesh Arrays *****
                                    Bytes            MB
      Character Arrays :                  0             0
      Integer Arrays   :           16272080            16
      Real Arrays      :           59535256            59
      Total            :           75807336            75
1source                                                                                                  print table 10
 values of defaulted or explicitly defined source variables
    cel        0.0000E+00
    sur        0.0000E+00
    tme        0.0000E+00
    dir        isotropic
    pos        0.0000E+00   0.0000E+00   0.0000E+00
    x          0.0000E+00
    y          0.0000E+00
    z          0.0000E+00
    rad        0.0000E+00
    ext        0.0000E+00
    axs        0.0000E+00   0.0000E+00   0.0000E+00
    vec        0.0000E+00   0.0000E+00   0.0000E+00
    ccc        0.0000E+00
    nrm        1.0000E+00
    ara        0.0000E+00
    wgt        1.0000E+00
    eff        1.0000E-02
    par        2.0000E+00
    tr         0.0000E+00
    bem        0.0000E+00   0.0000E+00   0.0000E+00
    bap        0.0000E+00   0.0000E+00   0.0000E+00
    loc        0.0000E+00   0.0000E+00   0.0000E+00
    dat        0.0000E+00   0.0000E+00   0.0000E+00
 probability distribution        1 for source variable erg
 unbiased discrete  distribution
 source        source           cumulative          probability
  entry         value           probability           of bin
    1       6.62000E-01        1.000000E+00        1.000000E+00
     the mean of source distribution        1 is  6.6200E-01
 order of sampling source variables.
 par pos erg tme wgt
1tally        4                                                                                          print table 30
+                                  tally "DetectorDose"
          tally type 4    track length estimate of particle flux.
          particle(s): photons
 cells     (3)
 dose function          interpolation mode is loglog
        energy         factor
      1.00000E-02    6.10000E-02
      1.50000E-02    8.30000E-01
      2.00000E-02    1.05000E+00
      3.00000E-02    8.10000E-01
      4.00000E-02    6.40000E-01
      5.00000E-02    5.50000E-01
      6.00000E-02    5.10000E-01
      8.00000E-02    5.30000E-01
      1.00000E-01    6.10000E-01
      1.50000E-01    8.90000E-01
      2.00000E-01    1.20000E+00
      3.00000E-01    1.80000E+00
      4.00000E-01    2.38000E+00
      5.00000E-01    2.93000E+00
      6.00000E-01    3.44000E+00
      8.00000E-01    4.38000E+00
      1.00000E+00    5.20000E+00
      1.50000E+00    6.90000E+00
      2.00000E+00    8.60000E+00
      3.00000E+00    1.11000E+01
      4.00000E+00    1.34000E+01
      5.00000E+00    1.55000E+01
      6.00000E+00    1.76000E+01
      8.00000E+00    2.16000E+01
      1.00000E+01    2.56000E+01
1material composition                                                                                    print table 40
 material
```

```
  number     component nuclide, atom fraction
        1            8016, 2.16586E-01       7014, 7.83414E-01
 material
  number     component nuclide, mass fraction
        1            8016, 2.40000E-01       7014, 7.60000E-01
1cell volumes and masses                                                                                    print table 50
              cell     atom          gram         input       calculated                                reason volume
                      density       density       volume        volume         mass       pieces    not calculated
        1        1  5.00638E-05   1.20000E-03   0.00000E+00   1.00000E+00   1.20000E-03      0
        2        2  5.00638E-05   1.20000E-03   0.00000E+00   1.24999E+08   1.49999E+05      0
        3        3  5.00638E-05   1.20000E-03   0.00000E+00   1.00000E+03   1.20000E+00      0
        4        4  0.00000E+00   0.00000E+00   0.00000E+00   0.00000E+00   0.00000E+00      0
        5        5  0.00000E+00   0.00000E+00   0.00000E+00   1.32651E+08   0.00000E+00      0
        6        6  0.00000E+00   0.00000E+00   0.00000E+00   0.00000E+00   0.00000E+00      0      infinite
1surface areas                                                                                              print table 50
           surface      input      calculated    reason area
                        area         area       not calculated
        1      100      0.00000E+00   2.60100E+05
        2      101      0.00000E+00   2.60100E+05
        3      102      0.00000E+00   2.60100E+05
        4      103      0.00000E+00   2.60100E+05
        5      104      0.00000E+00   2.60100E+05
        6      105      0.00000E+00   2.60100E+05
1cells                                                                                                      print table 60
                              atom        gram                                                  photon
              cell      mat   density     density     volume       mass            pieces importance
        1        1        1   5.00638E-05 1.20000E-03 1.00000E+00 1.20000E-03           0  1.0000E+00
        2        2        1   5.00638E-05 1.20000E-03 1.24999E+08 1.49999E+05           0  1.0000E+00
        3        3        1   5.00638E-05 1.20000E-03 1.00000E+03 1.20000E+00           0  1.0000E+00
        4        4        0   0.00000E+00 0.00000E+00 0.00000E+00 0.00000E+00           0  1.0000E+00
        5        5        0   0.00000E+00 0.00000E+00 1.32651E+08 0.00000E+00           0  1.0000E+00
        6        6        0   0.00000E+00 0.00000E+00 0.00000E+00 0.00000E+00           0  0.0000E+00
 total                                              2.57651E+08 1.50000E+05
1surfaces                                                                                                   print table 70
           surface        trans  type   surface coefficients
        1      100               px   -2.5500000E+02
        2      101               px    2.5500000E+02
        3      102               py   -2.5500000E+02
        4      103               py    2.5500000E+02
        5      104               pz   -2.5500000E+02
        6      105               pz    2.5500000E+02
    minimum source weight = 1.0000E+00    maximum source weight = 1.0000E+00
1cross-section tables                                                                                       print table 100
     XSDIR used: /home/dbo/MY_MCNP/MCNP_DATA/xsdir_mcnp6.2
     table    length
                      tables from file xdata/mcplib84
   7000.84p    3270  Update of MCPLIB04 Photon Compton Broadening Data For MCNP5 see LA-UR-    12-00018        01/03/12
                     Energy range:   1.00000E-03  to  1.00000E+05 MeV.
   8000.84p    3348  Update of MCPLIB04 Photon Compton Broadening Data For MCNP5 see LA-UR-    12-00018        01/03/12
                     Energy range:   1.00000E-03  to  1.00000E+05 MeV.
  total        6618
 maximum photon energy set to    100.0 mev (maximum electron energy)
                      tables from file xdata/el03
   7000.03e    2333                                                                                                 6/6/98
                     Energy range:   1.00000E-03  to  1.00000E+03 MeV.
   8000.03e    2333                                                                                                 6/6/98
                     Energy range:   1.00000E-03  to  1.00000E+03 MeV.
1particles and energy limits                                                                                print table 101
                       particle      maximum       smallest      largest       always        always
                       cutoff        particle      table         table         use table     use model
   particle type       energy        energy        maximum       maximum       below         above
    2  p    photon      1.0000E-03    1.0000E+02    1.0000E+05    1.0000E+05    1.0000E+36    1.0000E+36
    3  e    electron    1.0000E-03    1.0000E+02    1.0000E+02    1.0000E+02    1.0000E+36    1.0000E+36

 ************************************************************************************************************************
 dump no.    1 on file runtpe     nps =           0     coll =              0     ctm =        0.00   nrn =
    0
1starting mcrun.      cp0 =  5.79                                                                           print table 110
      freeair1
 master starting     191 MPI slave tasks with       1 threads each  06/04/22 09:29:52
 master set rendezvous nps =    10000000,  work chunks =   191    06/04/22 09:29:53


     nps    x          y          z          cell       surf     u          v          w        energy     weight      time

       1 -5.002E+01 -9.439E-02 -3.253E-01        5            9.832E-03  8.516E-01  5.241E-01  6.620E-01  1.000E+00  0.000E+00
         -5.002E+01 -9.439E-02 -3.253E-01        1          0 9.832E-03  8.516E-01  5.241E-01
       2 -4.999E+01 -4.367E-01  4.058E-01        5            1.166E-01  9.072E-01 -4.042E-01  6.620E-01  1.000E+00  0.000E+00
         -4.999E+01 -4.367E-01  4.058E-01        1          0 1.166E-01  9.072E-01 -4.042E-01
       3 -4.972E+01  4.531E-01  3.946E-01        5            4.273E-01  2.087E-01 -8.797E-01  6.620E-01  1.000E+00  0.000E+00
         -4.972E+01  4.531E-01  3.946E-01        1          0 4.273E-01  2.087E-01 -8.797E-01
       4 -5.014E+01  9.335E-03  2.489E-01        5            5.071E-02 -7.465E-01 -6.634E-01  6.620E-01  1.000E+00  0.000E+00
         -5.014E+01  9.335E-03  2.489E-01        1          0 5.071E-02 -7.465E-01 -6.634E-01
       5 -4.972E+01  2.405E-01  2.093E-01        5            9.732E-01  1.485E-01  1.754E-01  6.620E-01  1.000E+00  0.000E+00
         -4.972E+01  2.405E-01  2.093E-01        1          0 9.732E-01  1.485E-01  1.754E-01
       6 -4.960E+01  3.611E-01 -2.994E-01        5            2.014E-01  7.637E-01  6.134E-01  6.620E-01  1.000E+00  0.000E+00
         -4.960E+01  3.611E-01 -2.994E-01        1          0 2.014E-01  7.637E-01  6.134E-01
       7 -5.001E+01  2.735E-01 -1.997E-01        5            8.033E-01  5.256E-01 -2.801E-01  6.620E-01  1.000E+00  0.000E+00
         -5.001E+01  2.735E-01 -1.997E-01        1          0 8.033E-01  5.256E-01 -2.801E-01
       8 -5.030E+01 -2.437E-02 -2.201E-01        5            6.099E-01  7.825E-01 -1.255E-01  6.620E-01  1.000E+00  0.000E+00
         -5.030E+01 -2.437E-02 -2.201E-01        1          0 6.099E-01  7.825E-01 -1.255E-01
       9 -4.957E+01 -2.120E-01 -4.549E-01        5            8.505E-01 -1.422E-02  5.258E-01  6.620E-01  1.000E+00  0.000E+00
         -4.957E+01 -2.120E-01 -4.549E-01        1          0 8.505E-01 -1.422E-02  5.258E-01
      10 -4.954E+01  1.873E-01  7.555E-02        5            3.286E-01  8.839E-01 -3.328E-01  6.620E-01  1.000E+00  0.000E+00
         -4.954E+01  1.873E-01  7.555E-02        1          0 3.286E-01  8.839E-01 -3.328E-01
```

```
    11 -4.970E+01 -4.388E-01  1.394E-01       5          -5.964E-01  8.132E-02  7.986E-01  6.620E-01  1.000E+00  0.000E+00
       -4.970E+01 -4.388E-01  1.394E-01       1        0 -5.964E-01  8.132E-02  7.986E-01
    12 -5.039E+01 -1.825E-03  4.186E-01       5          -7.930E-01  1.277E-01  5.957E-01  6.620E-01  1.000E+00  0.000E+00
       -5.039E+01 -1.825E-03  4.186E-01       1        0 -7.930E-01  1.277E-01  5.957E-01
    13 -5.027E+01 -1.297E-01  4.671E-01       5          -3.340E-01 -8.236E-01  4.584E-01  6.620E-01  1.000E+00  0.000E+00
       -5.027E+01 -1.297E-01  4.671E-01       1        0 -3.340E-01 -8.236E-01  4.584E-01
    14 -4.979E+01 -3.487E-01  4.665E-01       5          -1.634E-01  1.026E-01  9.812E-01  6.620E-01  1.000E+00  0.000E+00
       -4.979E+01 -3.487E-01  4.665E-01       1        0 -1.634E-01  1.026E-01  9.812E-01
    15 -5.002E+01 -3.435E-01 -4.470E-01       5           8.614E-01  5.052E-01 -5.254E-02  6.620E-01  1.000E+00  0.000E+00
       -5.002E+01 -3.435E-01 -4.470E-01       1        0  8.614E-01  5.052E-01 -5.254E-02
    16 -4.956E+01  1.887E-01  1.968E-01       5           8.611E-01  2.932E-01 -4.153E-01  6.620E-01  1.000E+00  0.000E+00
       -4.956E+01  1.887E-01  1.968E-01       1        0  8.611E-01  2.932E-01 -4.153E-01
    17 -5.030E+01 -2.347E-02 -3.755E-01       5           4.144E-01  6.194E-01  6.668E-01  6.620E-01  1.000E+00  0.000E+00
       -5.030E+01 -2.347E-02 -3.755E-01       1        0  4.144E-01  6.194E-01  6.668E-01
    18 -5.027E+01  4.013E-01 -4.608E-01       5          -1.010E-01 -4.833E-01 -8.696E-01  6.620E-01  1.000E+00  0.000E+00
       -5.027E+01  4.013E-01 -4.608E-01       1        0 -1.010E-01 -4.833E-01 -8.696E-01
    19 -5.033E+01  4.019E-01  3.509E-01       5           5.726E-01 -4.964E-01 -6.524E-01  6.620E-01  1.000E+00  0.000E+00
       -5.033E+01  4.019E-01  3.509E-01       1        0  5.726E-01 -4.964E-01 -6.524E-01
    20 -5.027E+01  1.404E-01 -1.664E-01       5           1.376E-01 -2.790E-01  9.504E-01  6.620E-01  1.000E+00  0.000E+00
       -5.027E+01  1.404E-01 -1.664E-01       1        0  1.376E-01 -2.790E-01  9.504E-01
    21 -4.968E+01  4.498E-01 -3.161E-01       5           7.110E-01  4.583E-02  7.017E-01  6.620E-01  1.000E+00  0.000E+00
       -4.968E+01  4.498E-01 -3.161E-01       1        0  7.110E-01  4.583E-02  7.017E-01
    22 -5.009E+01 -1.905E-01  4.490E-02       5           2.294E-01  5.542E-01  8.002E-01  6.620E-01  1.000E+00  0.000E+00
       -5.009E+01 -1.905E-01  4.490E-02       1        0  2.294E-01  5.542E-01  8.002E-01
    23 -4.977E+01 -3.732E-01  4.191E-01       5           7.748E-01  6.006E-01  1.973E-01  6.620E-01  1.000E+00  0.000E+00
       -4.977E+01 -3.732E-01  4.191E-01       1        0  7.748E-01  6.006E-01  1.973E-01
    24 -4.953E+01  1.930E-01 -1.373E-01       5          -9.470E-01  1.771E-01  2.682E-01  6.620E-01  1.000E+00  0.000E+00
       -4.953E+01  1.930E-01 -1.373E-01       1        0 -9.470E-01  1.771E-01  2.682E-01
    25 -4.952E+01  2.208E-01 -3.929E-01       5          -5.388E-01 -7.206E-01 -4.364E-01  6.620E-01  1.000E+00  0.000E+00
       -4.952E+01  2.208E-01 -3.929E-01       1        0 -5.388E-01 -7.206E-01 -4.364E-01
    26 -5.048E+01 -2.871E-01  1.579E-01       5          -7.548E-02 -9.213E-01 -3.815E-01  6.620E-01  1.000E+00  0.000E+00
       -5.048E+01 -2.871E-01  1.579E-01       1        0 -7.548E-02 -9.213E-01 -3.815E-01
    27 -5.033E+01  2.537E-01  4.660E-01       5           5.076E-01  8.468E-01  1.592E-01  6.620E-01  1.000E+00  0.000E+00
       -5.033E+01  2.537E-01  4.660E-01       1        0  5.076E-01  8.468E-01  1.592E-01
    28 -5.005E+01  4.492E-01 -4.285E-01       5          -3.343E-01  9.301E-01  1.522E-01  6.620E-01  1.000E+00  0.000E+00
       -5.005E+01  4.492E-01 -4.285E-01       1        0 -3.343E-01  9.301E-01  1.522E-01
    29 -5.009E+01 -1.083E-01  3.411E-01       5           6.140E-01 -1.270E-01 -7.790E-01  6.620E-01  1.000E+00  0.000E+00
       -5.009E+01 -1.083E-01  3.411E-01       1        0  6.140E-01 -1.270E-01 -7.790E-01
    30 -4.953E+01 -1.775E-01 -5.569E-02       5           6.560E-01  5.281E-01  5.392E-01  6.620E-01  1.000E+00  0.000E+00
       -4.953E+01 -1.775E-01 -5.569E-02       1        0  6.560E-01  5.281E-01  5.392E-01
    31 -4.969E+01  1.140E-01  3.509E-01       5           5.550E-01  6.513E-01 -5.175E-01  6.620E-01  1.000E+00  0.000E+00
       -4.969E+01  1.140E-01  3.509E-01       1        0  5.550E-01  6.513E-01 -5.175E-01
    32 -5.038E+01  1.984E-01  3.247E-01       5           5.168E-04  6.735E-01  7.392E-01  6.620E-01  1.000E+00  0.000E+00
       -5.038E+01  1.984E-01  3.247E-01       1        0  5.168E-04  6.735E-01  7.392E-01
    33 -4.996E+01  2.594E-01 -4.499E-03       5           6.457E-01 -5.728E-01 -5.049E-01  6.620E-01  1.000E+00  0.000E+00
       -4.996E+01  2.594E-01 -4.499E-03       1        0  6.457E-01 -5.728E-01 -5.049E-01
    34 -4.995E+01  3.037E-01  2.686E-01       5           2.587E-01 -8.344E-01 -4.867E-01  6.620E-01  1.000E+00  0.000E+00
       -4.995E+01  3.037E-01  2.686E-01       1        0  2.587E-01 -8.344E-01 -4.867E-01
    35 -4.958E+01 -4.964E-02  4.491E-01       5           9.223E-01 -3.825E-01 -5.465E-02  6.620E-01  1.000E+00  0.000E+00
       -4.958E+01 -4.964E-02  4.491E-01       1        0  9.223E-01 -3.825E-01 -5.465E-02
    36 -5.012E+01 -2.001E-01  4.137E-01       5           7.839E-01 -1.706E-01 -5.970E-01  6.620E-01  1.000E+00  0.000E+00
       -5.012E+01 -2.001E-01  4.137E-01       1        0  7.839E-01 -1.706E-01 -5.970E-01
    37 -5.019E+01  3.937E-01 -3.967E-01       5          -9.634E-02 -7.625E-01  6.397E-01  6.620E-01  1.000E+00  0.000E+00
       -5.019E+01  3.937E-01 -3.967E-01       1        0 -9.634E-02 -7.625E-01  6.397E-01
    38 -5.000E+01 -3.803E-02  8.932E-02       5          -6.688E-01  6.967E-01 -2.594E-01  6.620E-01  1.000E+00  0.000E+00
       -5.000E+01 -3.803E-02  8.932E-02       1        0 -6.688E-01  6.967E-01 -2.594E-01
    39 -4.952E+01  8.463E-02  1.704E-01       5           3.169E-01 -1.596E-02 -9.483E-01  6.620E-01  1.000E+00  0.000E+00
       -4.952E+01  8.463E-02  1.704E-01       1        0  3.169E-01 -1.596E-02 -9.483E-01
    40 -4.975E+01  2.555E-01 -4.529E-01       5          -5.133E-01 -7.036E-01  4.914E-01  6.620E-01  1.000E+00  0.000E+00
       -4.975E+01  2.555E-01 -4.529E-01       1        0 -5.133E-01 -7.036E-01  4.914E-01
    41 -4.994E+01 -2.974E-02 -2.152E-01       5           3.537E-01  5.726E-01 -7.396E-01  6.620E-01  1.000E+00  0.000E+00
       -4.994E+01 -2.974E-02 -2.152E-01       1        0  3.537E-01  5.726E-01 -7.396E-01
    42 -5.024E+01 -3.584E-02  4.953E-01       5           6.318E-01  7.629E-01 -1.371E-01  6.620E-01  1.000E+00  0.000E+00
       -5.024E+01 -3.584E-02  4.953E-01       1        0  6.318E-01  7.629E-01 -1.371E-01
    43 -4.999E+01 -4.301E-01  2.415E-01       5           4.145E-01  1.022E-01 -9.043E-01  6.620E-01  1.000E+00  0.000E+00
       -4.999E+01 -4.301E-01  2.415E-01       1        0  4.145E-01  1.022E-01 -9.043E-01
    44 -4.980E+01 -2.996E-01  1.065E-01       5           8.791E-01  4.720E-01 -6.683E-02  6.620E-01  1.000E+00  0.000E+00
       -4.980E+01 -2.996E-01  1.065E-01       1        0  8.791E-01  4.720E-01 -6.683E-02
    45 -5.038E+01 -1.571E-01 -3.414E-01       5          -7.749E-01  6.188E-01 -1.291E-01  6.620E-01  1.000E+00  0.000E+00
       -5.038E+01 -1.571E-01 -3.414E-01       1        0 -7.749E-01  6.188E-01 -1.291E-01
    46 -4.957E+01  2.679E-01  2.510E-02       5           1.895E-01 -5.774E-01 -7.942E-01  6.620E-01  1.000E+00  0.000E+00
       -4.957E+01  2.679E-01  2.510E-02       1        0  1.895E-01 -5.774E-01 -7.942E-01
    47 -5.021E+01 -8.502E-03  4.494E-01       5          -3.241E-01  2.180E-01 -9.205E-01  6.620E-01  1.000E+00  0.000E+00
       -5.021E+01 -8.502E-03  4.494E-01       1        0 -3.241E-01  2.180E-01 -9.205E-01
    48 -4.953E+01  1.654E-01  4.284E-01       5           2.426E-01  9.452E-01  2.183E-01  6.620E-01  1.000E+00  0.000E+00
       -4.953E+01  1.654E-01  4.284E-01       1        0  2.426E-01  9.452E-01  2.183E-01
    49 -4.971E+01  4.664E-01 -4.631E-01       5          -4.052E-01 -7.229E-02  9.114E-01  6.620E-01  1.000E+00  0.000E+00
       -4.971E+01  4.664E-01 -4.631E-01       1        0 -4.052E-01 -7.229E-02  9.114E-01
    50 -5.023E+01 -1.196E-01 -3.327E-01       5          -9.845E-01  1.750E-01  1.182E-02  6.620E-01  1.000E+00  0.000E+00
       -5.023E+01 -1.196E-01 -3.327E-01       1        0 -9.845E-01  1.750E-01  1.182E-02
 master set rendezvous nps =    20000000,  work chunks =   191    06/04/22 09:30:20
 master set rendezvous nps =    30000000,  work chunks =   191    06/04/22 09:30:47
 master set rendezvous nps =    40000000,  work chunks =   191    06/04/22 09:31:14
 master set rendezvous nps =    50000000,  work chunks =   191    06/04/22 09:31:41
 master set rendezvous nps =    60000000,  work chunks =   191    06/04/22 09:32:08
 master set rendezvous nps =    70000000,  work chunks =   191    06/04/22 09:32:35
 master set rendezvous nps =    80000000,  work chunks =   191    06/04/22 09:33:02
 master set rendezvous nps =    90000000,  work chunks =   191    06/04/22 09:33:29
 master set rendezvous nps =   100000000,  work chunks =   191    06/04/22 09:33:56
1problem summary
      run terminated when   100000000  particle histories were done.
+                                                                                                    06/04/22 09:34:23
 =====>    1331.11 M histories/hr    (based on wall-clock time in mcrun)
      freeair1     probid =  06/04/22 09:24:05
 photon creation     tracks      weight        energy           photon loss         tracks      weight        energy
```

```
                                (per source particle)                                                                (per source particle)
 source           100000000    1.0000E+00    6.6200E-01          escape           100022917    1.0002E+00    6.5496E-01
 nucl. interaction        0    0.            0.                  energy cutoff            0    0.            1.6813E-07
 particle decay           0    0.            0.                  time cutoff              0    0.            0.
 weight window            0    0.            0.                  weight window            0    0.            0.
 cell importance          0    0.            0.                  cell importance          0    0.            0.
 weight cutoff            0    0.            0.                  weight cutoff            0    0.            0.
 e or t importance        0    0.            0.                  e or t importance        0    0.            0.
 dxtran                   0    0.            0.                  dxtran                   0    0.            0.
 forced collisions        0    0.            0.                  forced collisions        0    0.            0.
 exp. transform           0    0.            0.                  exp. transform           0    0.            0.
 from neutrons            0    0.            0.                  compton scatter          0    0.            7.0469E-03
 bremsstrahlung       58826    5.8826E-04    1.1676E-05          capture              35909    3.5909E-04    3.5055E-06
 p-annihilation           0    0.            0.                  pair production          0    0.            0.
 photonuclear             0    0.            0.                  photonuclear abs         0    0.            0.
 electron x-rays          0    0.            0.                  loss to photofis         0    0.            0.
 compton fluores          0    0.            0.
 muon capt fluores        0    0.            0.
 1st fluorescence         0    0.            0.
 2nd fluorescence         0    0.            0.
 cerenkov                 0    0.            0.
 (gamma,xgamma)           0    0.            0.
 tabular sampling         0    0.            0.
 prompt photofis          0    0.            0.
     total        100058826    1.0006E+00    6.6201E-01              total        100058826    1.0006E+00    6.6201E-01
   number of photons banked                 58826        average time of (shakes)              cutoffs
   photon tracks per source particle      1.0006E+00       escape            1.0362E+00          tco   1.0000E+33
   photon collisions per source particle  2.8754E-02       capture           5.6158E-01          eco   1.0000E-03
   total photon collisions                 2875428         capture or escape 1.0361E+00          wc1  -5.0000E-01
                                                           any termination   1.0361E+00          wc2  -2.5000E-01

 computer time so far in this run   872.03 minutes          maximum number ever in bank         2
 computer time in mcrun             835.77 minutes          bank overflows to backup file       0
 source particles per minute           1.1965E+05
 random numbers generated              2896106830          most random numbers used was         888 in history    32544927
 range of sampled source weights = 1.0000E+00 to 1.0000E+00
 number of histories processed by each MPI task
          0       523560       523560       523560       523560       523560       523560       523560       523560       523560
     523560       523560       523560       523560       523560       523560       523560       523560       523560       523560
     523560       523560       523560       523560       523560       523560       523560       523560       523560       523560
     523560       523560       523560       523560       523560       523560       523560       523560       523560       523560
     523560       523560       523560       523560       523560       523560       523560       523560       523570       523560
     523560       523560       523560       523560       523560       523560       523560       523560       523560       523560
     523560       523560       523560       523560       523560       523560       523560       523560       523560       523560
     523560       523560       523560       523560       523560       523560       523560       523560       523560       523560
     523560       523560       523560       523560       523560       523560       523560       523560       523560       523560
     523560       523560       523560       523560       523560       523560       523560       523560       523560       523560
     523560       523560       523560       523560       523560       523560       523560       523560       523560       523560
     523560       523560       523560       523560       523560       523560       523560       523560       523560       523560
     523560       523560       523560       523560       523560       523560       523560       523560       523560       523560
     523560       523560       523560       523560       523560       523560       523560       523560       523560       523560
     523560       523560       523560       523560       523570       523560       523560       523560       523560       523560
     523560       523560       523560       523560       523560       523560       523560       523560       523560       523560
     523560       523560       523560       523560       523560       523560       523560       523560       523560       523560
     523560       523560       523560       523560       523560       523560       523560       523560       523560       523560
     523560       523560       523560       523560       523560       523560       523560       523560       523560       523560
     523560       523570
1source distribution frequency tables                                                                                  print table 170
 the expected values below do not include the effect of the rejection loop which samples position.
 source distribution   1  for erg
                                        number                                          weight
            source
   n          value         sampled      expected  sampled/expected      sampled      expected  sampled/expected
   1      6.62000E-01      1.0000E+00   1.0000E+00   1.0000E+00         1.0000E+00   1.0000E+00   1.0000E+00
 total                    1.0000E+00   1.0000E+00   1.0000E+00         1.0000E+00   1.0000E+00   1.0000E+00
1the following cells are bounded by cells with photon   importances                                                   print table 120
 that may be different by more than a factor of four.
                      maximum                                  minimum
  cell     importance     neighbor     importance   ratio     neighbor     importance   ratio
       1     no data available yet for this cell.
       2     no data available yet for this cell.
       3     no data available yet for this cell.
       4     no data available yet for this cell.
 End of importance function analysis
1photon   activity in each cell                                                                                       print table 126
                      tracks     population   collisions   collisions     number        flux        average      average
            cell    entering                               * weight     weighted     weighted   track weight   track mfp
                                                         (per history)    energy       energy     (relative)      (cm)
       1        1   100001415    100000080         4152    4.1520E-05   6.6198E-01   6.6198E-01   1.0000E+00   1.0802E+04
       2        2   100089909    100058820      2871198    2.8712E-02   6.5574E-01   6.5574E-01   1.0000E+00   1.0749E+04
       3        3       88419        88411           78    7.8000E-07   6.5678E-01   6.5678E-01   1.0000E+00   1.0758E+04
       4        4   100022917    100022917            0    0.0000E+00   6.5342E-01   6.5342E-01   1.0000E+00   0.0000E+00
       5        5           0            0            0    0.0000E+00   0.0000E+00   0.0000E+00   0.0000E+00   0.0000E+00
          total     300202660    300170228      2875428    2.8754E-02
1photon   activity in each repeated structure / lattice element                                                       print table 128
      source    entering  collisions        path
   100000000   100001415        4152     1 <    5
           0   100089909     2871198     2 <    5
           0       88419          78     3 <    5
           0   100022917           0     4 <    5
           0           0           0     6
   100000000   300202660     2875428
         print table 128 requires          68 decimal words of dynamically allocated storage.
1photon   weight balance in each cell                                                                                 print table 130
       cell index        1           2           3           4           5
      cell number        1           2           3           4           5       total
```

```
 external events:
          entering  1.4150E-05  1.0009E+00  8.8419E-04  1.0002E+00  0.0000E+00  2.0020E+00
            source  1.0000E+00  0.0000E+00  0.0000E+00  0.0000E+00  0.0000E+00  1.0000E+00
     energy cutoff  0.0000E+00  0.0000E+00  0.0000E+00  0.0000E+00  0.0000E+00  0.0000E+00
       time cutoff  0.0000E+00  0.0000E+00  0.0000E+00  0.0000E+00  0.0000E+00  0.0000E+00
           exiting -1.0000E+00 -1.0011E+00 -8.8420E-04 -1.0002E+00  0.0000E+00 -3.0023E+00
                   ----------  ----------  ----------  ----------  ----------  ----------
             total -7.4000E-07 -2.2842E-04 -1.0000E-08  0.0000E+00  0.0000E+00 -2.2917E-04
 variance reduction events:
     weight window  0.0000E+00  0.0000E+00  0.0000E+00  0.0000E+00  0.0000E+00  0.0000E+00
   cell importance  0.0000E+00  0.0000E+00  0.0000E+00  0.0000E+00  0.0000E+00  0.0000E+00
     weight cutoff  0.0000E+00  0.0000E+00  0.0000E+00  0.0000E+00  0.0000E+00  0.0000E+00
 e or t importance  0.0000E+00  0.0000E+00  0.0000E+00  0.0000E+00  0.0000E+00  0.0000E+00
            dxtran  0.0000E+00  0.0000E+00  0.0000E+00  0.0000E+00  0.0000E+00  0.0000E+00
 forced collisions  0.0000E+00  0.0000E+00  0.0000E+00  0.0000E+00  0.0000E+00  0.0000E+00
    exp. transform  0.0000E+00  0.0000E+00  0.0000E+00  0.0000E+00  0.0000E+00  0.0000E+00
                    ----------  ----------  ----------  ----------  ----------  ----------
             total  0.0000E+00  0.0000E+00  0.0000E+00  0.0000E+00  0.0000E+00  0.0000E+00
 physical events:
     from neutrons  0.0000E+00  0.0000E+00  0.0000E+00  0.0000E+00  0.0000E+00  0.0000E+00
    bremsstrahlung  8.0000E-07  5.8745E-04  1.0000E-08  0.0000E+00  0.0000E+00  5.8826E-04
           capture -6.0000E-08 -3.5903E-04  0.0000E+00  0.0000E+00  0.0000E+00 -3.5909E-04
    p-annihilation  0.0000E+00  0.0000E+00  0.0000E+00  0.0000E+00  0.0000E+00  0.0000E+00
   pair production  0.0000E+00  0.0000E+00  0.0000E+00  0.0000E+00  0.0000E+00  0.0000E+00
      photonuclear  0.0000E+00  0.0000E+00  0.0000E+00  0.0000E+00  0.0000E+00  0.0000E+00
 photonuclear abs  0.0000E+00  0.0000E+00  0.0000E+00  0.0000E+00  0.0000E+00  0.0000E+00
   electron x-rays  0.0000E+00  0.0000E+00  0.0000E+00  0.0000E+00  0.0000E+00  0.0000E+00
   compton fluores  0.0000E+00  0.0000E+00  0.0000E+00  0.0000E+00  0.0000E+00  0.0000E+00
 muon capt fluores  0.0000E+00  0.0000E+00  0.0000E+00  0.0000E+00  0.0000E+00  0.0000E+00
      fluorescence  0.0000E+00  0.0000E+00  0.0000E+00  0.0000E+00  0.0000E+00  0.0000E+00
          cerenkov  0.0000E+00  0.0000E+00  0.0000E+00  0.0000E+00  0.0000E+00  0.0000E+00
        decay gain  0.0000E+00  0.0000E+00  0.0000E+00  0.0000E+00  0.0000E+00  0.0000E+00
 nucl. interaction  0.0000E+00  0.0000E+00  0.0000E+00  0.0000E+00  0.0000E+00  0.0000E+00
  tabular sampling  0.0000E+00  0.0000E+00  0.0000E+00  0.0000E+00  0.0000E+00  0.0000E+00
      photofission  0.0000E+00  0.0000E+00  0.0000E+00  0.0000E+00  0.0000E+00  0.0000E+00
  loss to photofis  0.0000E+00  0.0000E+00  0.0000E+00  0.0000E+00  0.0000E+00  0.0000E+00
                    ----------  ----------  ----------  ----------  ----------  ----------
             total  7.4000E-07  2.2842E-04  1.0000E-08  0.0000E+00  0.0000E+00  2.2917E-04
                    ----------  ----------  ----------  ----------  ----------  ----------
             total  0.0000E+00  0.0000E+00  0.0000E+00  0.0000E+00  0.0000E+00  0.0000E+00

1photoatomic activity of each nuclide in each cell, per source particle                                                print table 140
     cell     cell   nuclides     atom       total  collisions   wgt. lost   weight of       total   weight of      total    weight of
    index     name            fraction  collisions    * weight  to capture   pair prod  incoherent  incoherent   coherent    coherent
        1        1   8000.84p 2.17E-01         971  9.7100E-06  0.0000E+00  0.0000E+00         970  9.7000E-06          1  1.0000E-08
                     7000.84p 7.83E-01        3181  3.1810E-05  6.0000E-08  0.0000E+00        3174  3.1740E-05          1  1.0000E-08
        2        2   8000.84p 2.17E-01      692693  6.9269E-03  1.1594E-04  0.0000E+00      679513  6.7951E-03       1586  1.5860E-05
                     7000.84p 7.83E-01     2178505  2.1785E-02  2.4309E-04  0.0000E+00     2150381  2.1504E-02       3815  3.8150E-05
        3        3   8000.84p 2.17E-01          18  1.8000E-07  0.0000E+00  0.0000E+00          18  1.8000E-07          0  0.0000E+00
                     7000.84p 7.83E-01          60  6.0000E-07  0.0000E+00  0.0000E+00          60  6.0000E-07          0  0.0000E+00
             total                        2875428  2.8754E-02  3.5909E-04  0.0000E+00     2834116  2.8341E-02       5403  5.4030E-05
       total over all cells by nuclide       total  collisions   wgt. lost   weight of       total   weight of      total    weight of
                                        collisions    * weight  to capture   pair prod  incoherent  incoherent   coherent    coherent
                     7000.84p             2181746  2.1817E-02  2.4315E-04  0.0000E+00     2153615  2.1536E-02       3816  3.8160E-05
                     8000.84p              693682  6.9368E-03  1.1594E-04  0.0000E+00      680501  6.8050E-03       1587  1.5870E-05
1tally        4        nps =   100000000
+                                  tally "DetectorDose"
           tally type 4    track length estimate of particle flux.
           particle(s): photons
           this tally is modified by dose function DE4 and DF4.
           volumes
                   cell:       3
                         1.00000E+03

 cell  3
                  2.95651E-05 0.0035
 ============================================================================================================================================
          results of 10 statistical checks for the estimated answer for the tally fluctuation chart (tfc) bin of tally        4
 tfc bin     --mean--      ---------relative error---------      ----variance of the variance----      --figure of merit--     -pdf-
 behavior    behavior      value   decrease   decrease rate      value   decrease   decrease rate       value     behavior     slope
 desired      random       <0.10      yes      1/sqrt(nps)       <0.10      yes        1/nps          constant    random      >3.00
 observed     random        0.00      yes          yes            0.00      yes         yes           constant    random       3.83
 passed?        yes          yes      yes          yes             yes      yes         yes             yes         yes          yes
 ============================================================================================================================================
 this tally meets the statistical criteria used to form confidence intervals: check the tally fluctuation chart to verify.
 the results in other bins associated with this tally may not meet these statistical criteria.
 ----- estimated confidence intervals:  -----
 estimated asymmetric confidence interval(1,2,3 sigma): 2.9462E-05 to 2.9668E-05; 2.9359E-05 to 2.9772E-05; 2.9256E-05 to
2.9875E-05
 estimated  symmetric confidence interval(1,2,3 sigma): 2.9462E-05 to 2.9668E-05; 2.9359E-05 to 2.9771E-05; 2.9256E-05 to
2.9875E-05
1analysis of the results in the tally fluctuation chart bin (tfc) for tally 4 with nps = 100000000           print table 160
 normed average tally per history  = 2.95651E-05          unnormed average tally per history  = 2.95651E-02
 estimated tally relative error    = 0.0035               estimated variance of the variance  = 0.0000
 relative error from zero tallies  = 0.0034               relative error from nonzero scores  = 0.0009
 number of nonzero history tallies =       88410          efficiency for the nonzero tallies  = 0.0009
 history number of largest  tally  =    46854439          largest  unnormalized history tally = 4.85509E+01
 (largest  tally)/(average tally)  = 1.64217E+03          (largest  tally)/(avg nonzero tally)= 1.45184E+00
 (confidence interval shift)/mean  = 0.0000               shifted confidence interval center  = 2.95653E-05
 if the largest  history score sampled so far were to occur on the next history, the tfc bin quantities would change as follows:
      estimated quantities           value at nps           value at nps+1           value(nps+1)/value(nps)-1.
      mean                            2.95651E-05            2.95656E-05                    0.000016
      relative error                  3.48931E-03            3.48929E-03                   -0.000005
      variance of the variance        1.27196E-05            1.27195E-05                   -0.000006
      shifted center                  2.95653E-05            2.95653E-05                    0.000000
      figure of merit                 9.82734E+01            9.82744E+01                    0.000011
 the estimated inverse power slope of the  19 largest  tallies starting at 3.74688E+01 is 3.8293
```

```
 the empirical history score probability density function appears to be increasing at the largest  history scores:
 please examine. see print table 161.
 the large score tail of the empirical history score probability density function appears to have no unsampled regions.
 fom = (histories/minute)*(f(x) signal-to-noise ratio)**2 = (1.197E+05)*( 2.866E-02)**2 = (1.197E+05)*(8.213E-04) = 9.827E+01
1unnormed tally density for tally 4          nonzero tally mean(m) = 3.344E+01   nps = 100000000             print table 161
 abscissa              ordinate   log plot of tally probability density function in tally fluctuation chart bin(d=decade,slope=
3.8)
  tally  number num den log den:d----------------------d----------------------d----------------------d----------------------d--
 2.00-03      1 2.44-05  -4.613 **********************|**********************|**********************|*************          |
 2.51-03      1 1.94-05  -4.713 **********************|**********************|**********************|***********            |
 3.16-03      1 1.54-05  -4.813 **********************|**********************|**********************|********               |
 3.98-03      0 0.00+00   0.000                      |                      |                      |                       |
 5.01-03      0 0.00+00   0.000                      |                      |                      |                       |
 6.31-03      0 0.00+00   0.000                      |                      |                      |                       |
 7.94-03      0 0.00+00   0.000                      |                      |                      |                       |
 1.00-02      6 2.92-05  -4.535 **********************|**********************|**********************|***************        |
 1.26-02      1 3.86-06  -5.413 **********************|**********************|*****************     |                       |
 1.58-02      3 9.20-06  -5.036 **********************|**********************|**********************|***                    |
 2.00-02      3 7.31-06  -5.136 **********************|**********************|**********************|                       |
 2.51-02      1 1.94-06  -5.713 **********************|**********************|***********           |                       |
 3.16-02      3 4.61-06  -5.336 **********************|**********************|********************  |                       |
 3.98-02      4 4.89-06  -5.311 **********************|**********************|********************  |                       |
 5.01-02      6 5.82-06  -5.235 **********************|**********************|********************** |                       |
 6.31-02     11 8.48-06  -5.072 **********************|**********************|**********************|**                     |
 7.94-02      6 3.67-06  -5.435 **********************|**********************|*****************       |                       |
 1.00-01     12 5.83-06  -5.234 **********************|**********************|********************** |                       |
 1.26-01     11 4.25-06  -5.372 **********************|**********************|*******************     |                       |
 1.58-01     20 6.14-06  -5.212 **********************|**********************|**********************|                       |
 2.00-01     19 4.63-06  -5.334 **********************|**********************|********************  |                       |
 2.51-01     37 7.16-06  -5.145 **********************|**********************|**********************|                       |
 3.16-01     38 5.84-06  -5.233 **********************|**********************|********************** |                       |
 3.98-01     41 5.01-06  -5.300 **********************|**********************|********************  |                       |
 5.01-01     61 5.92-06  -5.228 **********************|**********************|********************** |                       |
 6.31-01     86 6.63-06  -5.179 **********************|**********************|**********************|                       |
 7.94-01     92 5.63-06  -5.249 **********************|**********************|********************** |                       |
 1.00+00    117 5.69-06  -5.245 **********************|**********************|********************** |                       |
 1.26+00    141 5.45-06  -5.264 **********************|**********************|********************  |                       |
 1.58+00    203 6.23-06  -5.206 **********************|**********************|**********************|                       |
 2.00+00    245 5.97-06  -5.224 **********************|**********************|********************** |                       |
 2.51+00    269 5.21-06  -5.283 **********************|**********************|********************  |                       |
 3.16+00    381 5.86-06  -5.232 **********************|**********************|********************** |                       |
 3.98+00    457 5.58-06  -5.253 **********************|**********************|********************** |                       |
 5.01+00    564 5.47-06  -5.262 **********************|**********************|********************  |                       |
 6.31+00    670 5.16-06  -5.287 **********************|**********************|********************  |                       |
 7.94+00    821 5.03-06  -5.299 **********************|**********************|********************  |                       |
 1.00+01   1065 5.18-06  -5.286 **********************|**********************|********************  |                       |
 1.26+01   1350 5.21-06  -5.283 **********************|**********************|********************  |                       |
 1.58+01   1622 4.98-06  -5.303 **********************|**********************|********************  |                       |
 2.00+01   1865 4.54-06  -5.342 **********************|**********************|******************    |                       |
 2.51+01   2275 4.40-06  -5.356 **********************|**********************|******************    |                       |
 3.16+01   2655 4.08-06  -5.389 **********************|**********************|******************    |                       |
 3.98+01  73238 8.94-05  -4.048 mmmmmmmmmmmmmmmmmmmmmmmmmm|mmmmmmmmmmmmmmmmmmmmmmmmmm|mmmmmmmmmmmmmmmmmmmmmmmmmm|mmmmmmmmmmmmmmmmmmmmmmmmmm|ms
 5.01+01      8 7.76-09  -8.110 *                      |                      |                      |                     s |
  total   88410 8.84-04         d----------------------d----------------------d----------------------d----------------------d--
1cumulative tally number for tally 4         nonzero tally mean(m) = 3.344E+01   nps = 100000000           print table 162
   abscissa     cum   ordinate    plot of the cumulative number of tallies in the tally fluctuation chart bin from 0 to 100 percent
    tally      number  cum pct:--------10--------20--------30--------40--------50--------60--------70--------80--------90-------100
 1.99526E-03        1    0.001|         |         |         |         |         |         |         |         |         |         |
 2.51189E-03        2    0.002|         |         |         |         |         |         |         |         |         |         |
 3.16228E-03        3    0.003|         |         |         |         |         |         |         |         |         |         |
 3.98107E-03        3    0.003|         |         |         |         |         |         |         |         |         |         |
 5.01187E-03        3    0.003|         |         |         |         |         |         |         |         |         |         |
 6.30957E-03        3    0.003|         |         |         |         |         |         |         |         |         |         |
 7.94328E-03        3    0.003|         |         |         |         |         |         |         |         |         |         |
 1.00000E-02        9    0.010|         |         |         |         |         |         |         |         |         |         |
 1.25893E-02       10    0.011|         |         |         |         |         |         |         |         |         |         |
 1.58489E-02       13    0.015|         |         |         |         |         |         |         |         |         |         |
 1.99526E-02       16    0.018|         |         |         |         |         |         |         |         |         |         |
 2.51189E-02       17    0.019|         |         |         |         |         |         |         |         |         |         |
 3.16228E-02       20    0.023|         |         |         |         |         |         |         |         |         |         |
 3.98107E-02       24    0.027|         |         |         |         |         |         |         |         |         |         |
 5.01187E-02       30    0.034|         |         |         |         |         |         |         |         |         |         |
 6.30957E-02       41    0.046|         |         |         |         |         |         |         |         |         |         |
 7.94328E-02       47    0.053|         |         |         |         |         |         |         |         |         |         |
 1.00000E-01       59    0.067|         |         |         |         |         |         |         |         |         |         |
 1.25893E-01       70    0.079|         |         |         |         |         |         |         |         |         |         |
 1.58489E-01       90    0.102|         |         |         |         |         |         |         |         |         |         |
 1.99526E-01      109    0.123|         |         |         |         |         |         |         |         |         |         |
 2.51189E-01      146    0.165|         |         |         |         |         |         |         |         |         |         |
 3.16228E-01      184    0.208|         |         |         |         |         |         |         |         |         |         |
 3.98107E-01      225    0.254|         |         |         |         |         |         |         |         |         |         |
 5.01187E-01      286    0.323|         |         |         |         |         |         |         |         |         |         |
 6.30957E-01      372    0.421|         |         |         |         |         |         |         |         |         |         |
 7.94328E-01      464    0.525|*        |         |         |         |         |         |         |         |         |         |
 1.00000E+00      581    0.657|*        |         |         |         |         |         |         |         |         |         |
 1.25893E+00      722    0.817|*        |         |         |         |         |         |         |         |         |         |
 1.58489E+00      925    1.046|*        |         |         |         |         |         |         |         |         |         |
 1.99526E+00     1170    1.323|*        |         |         |         |         |         |         |         |         |         |
 2.51189E+00     1439    1.628|**       |         |         |         |         |         |         |         |         |         |
 3.16228E+00     1820    2.059|**       |         |         |         |         |         |         |         |         |         |
 3.98107E+00     2277    2.576|***      |         |         |         |         |         |         |         |         |         |
 5.01187E+00     2841    3.213|***      |         |         |         |         |         |         |         |         |         |
 6.30957E+00     3511    3.971|****     |         |         |         |         |         |         |         |         |         |
 7.94328E+00     4332    4.900|*****    |         |         |         |         |         |         |         |         |         |
 1.00000E+01     5397    6.105|******   |         |         |         |         |         |         |         |         |         |
 1.25893E+01     6747    7.631|******** |         |         |         |         |         |         |         |         |         |
 1.58489E+01     8369    9.466|*********|         |         |         |         |         |         |         |         |         |
 1.99526E+01    10234   11.576|*********|**       |         |         |         |         |         |         |         |         |
 2.51189E+01    12509   14.149|*********|****     |         |         |         |         |         |         |         |         |
 3.16228E+01    15164   17.152|*********|*******  |         |         |         |         |         |         |         |         |
 3.98107E+01    88402   99.991|mmmmmmmmmm|mmmmmmmmmm|mmmmmmmmmm|mmmmmmmmmm|mmmmmmmmmm|mmmmmmmmmm|mmmmmmmmmm|mmmmmmmmmm|mmmmmmmmmm|
 5.01187E+01    88410  100.000|*********|*********|*********|*********|*********|*********|*********|*********|*********|*********|
    total       88410  100.000:--------10--------20--------30--------40--------50--------60--------70--------80--------90-------100
```

```
1cumulative unnormed tally for tally 4         nonzero tally mean(m) = 3.344E+01   nps = 100000000          print table 162
  abscissa     cum    ordinate               plot of the cumulative tally in the tally fluctuation chart bin from 0 to 100 percent
   tally    tally/nps  cum pct:--------10--------20--------30--------40--------50--------60--------70--------80--------90-------100
 1.995E-03  1.600E-11    0.000|         |         |         |         |         |         |         |         |         |         |
 2.512E-03  3.641E-11    0.000|         |         |         |         |         |         |         |         |         |         |
 3.162E-03  6.725E-11    0.000|         |         |         |         |         |         |         |         |         |         |
 3.981E-03  6.725E-11    0.000|         |         |         |         |         |         |         |         |         |         |
 5.012E-03  6.725E-11    0.000|         |         |         |         |         |         |         |         |         |         |
 6.310E-03  6.725E-11    0.000|         |         |         |         |         |         |         |         |         |         |
 7.943E-03  6.725E-11    0.000|         |         |         |         |         |         |         |         |         |         |
 1.000E-02  6.007E-10    0.000|         |         |         |         |         |         |         |         |         |         |
 1.259E-02  7.195E-10    0.000|         |         |         |         |         |         |         |         |         |         |
 1.585E-02  1.129E-09    0.000|         |         |         |         |         |         |         |         |         |         |
 1.995E-02  1.665E-09    0.000|         |         |         |         |         |         |         |         |         |         |
 2.512E-02  1.875E-09    0.000|         |         |         |         |         |         |         |         |         |         |
 3.162E-02  2.732E-09    0.000|         |         |         |         |         |         |         |         |         |         |
 3.981E-02  4.158E-09    0.000|         |         |         |         |         |         |         |         |         |         |
 5.012E-02  7.018E-09    0.000|         |         |         |         |         |         |         |         |         |         |
 6.310E-02  1.325E-08    0.000|         |         |         |         |         |         |         |         |         |         |
 7.943E-02  1.753E-08    0.000|         |         |         |         |         |         |         |         |         |         |
 1.000E-01  2.818E-08    0.000|         |         |         |         |         |         |         |         |         |         |
 1.259E-01  4.078E-08    0.000|         |         |         |         |         |         |         |         |         |         |
 1.585E-01  6.865E-08    0.000|         |         |         |         |         |         |         |         |         |         |
 1.995E-01  1.017E-07    0.000|         |         |         |         |         |         |         |         |         |         |
 2.512E-01  1.849E-07    0.001|         |         |         |         |         |         |         |         |         |         |
 3.162E-01  2.930E-07    0.001|         |         |         |         |         |         |         |         |         |         |
 3.981E-01  4.400E-07    0.001|         |         |         |         |         |         |         |         |         |         |
 5.012E-01  7.140E-07    0.002|         |         |         |         |         |         |         |         |         |         |
 6.310E-01  1.204E-06    0.004|         |         |         |         |         |         |         |         |         |         |
 7.943E-01  1.864E-06    0.006|         |         |         |         |         |         |         |         |         |         |
 1.000E+00  2.908E-06    0.010|         |         |         |         |         |         |         |         |         |         |
 1.259E+00  4.498E-06    0.015|         |         |         |         |         |         |         |         |         |         |
 1.585E+00  7.392E-06    0.025|         |         |         |         |         |         |         |         |         |         |
 1.995E+00  1.177E-05    0.040|         |         |         |         |         |         |         |         |         |         |
 2.512E+00  1.781E-05    0.060|         |         |         |         |         |         |         |         |         |         |
 3.162E+00  2.862E-05    0.097|         |         |         |         |         |         |         |         |         |         |
 3.981E+00  4.488E-05    0.152|         |         |         |         |         |         |         |         |         |         |
 5.012E+00  7.022E-05    0.238|         |         |         |         |         |         |         |         |         |         |
 6.310E+00  1.080E-04    0.365|         |         |         |         |         |         |         |         |         |         |
 7.943E+00  1.665E-04    0.563|*        |         |         |         |         |         |         |         |         |         |
 1.000E+01  2.621E-04    0.887|*        |         |         |         |         |         |         |         |         |         |
 1.259E+01  4.147E-04    1.403|*        |         |         |         |         |         |         |         |         |         |
 1.585E+01  6.450E-04    2.182|**       |         |         |         |         |         |         |         |         |         |
 1.995E+01  9.787E-04    3.310|***      |         |         |         |         |         |         |         |         |         |
 2.512E+01  1.491E-03    5.042|*****    |         |         |         |         |         |         |         |         |         |
 3.162E+01  2.245E-03    7.594|******** |         |         |         |         |         |         |         |         |         |
 3.981E+01  2.956E-02   99.988|mmmmmmmmm|mmmmmmmmm|mmmmmmmmm|mmmmmmmmm|mmmmmmmmm|mmmmmmmmm|mmmmmmmmm|mmmmmmmmm|mmmmmmmmm|mmmmmmmmm|
 5.012E+01  2.957E-02  100.000|*********|*********|*********|*********|*********|*********|*********|*********|*********|*********|
   total  2.95651E-02  100.000:--------10--------20--------30--------40--------50--------60--------70--------80--------90-------100
1status of the statistical checks used to form confidence intervals for the mean for each tally bin
 tally   result of statistical checks for the tfc bin (the first check not passed is listed) and error magnitude check for all
bins
        4   passed the 10 statistical checks for the tally fluctuation chart bin result
         passed all bin error check:     1 tally bins all have relative errors less than 0.10 with no zero bins
 the 10 statistical checks are only for the tally fluctuation chart bin and do not apply to other tally bins.
1tally fluctuation charts
                          tally        4
          nps      mean     error    vov  slope    fom
     10000000   2.9426E-05 0.0111 0.0001 10.0      98
     20000000   2.9540E-05 0.0078 0.0001 10.0      98
     30000000   2.9600E-05 0.0064 0.0000 10.0      98
     40000000   2.9648E-05 0.0055 0.0000 10.0      99
     50000000   2.9548E-05 0.0049 0.0000  1.6      98
     60000000   2.9521E-05 0.0045 0.0000  1.7      98
     70000000   2.9543E-05 0.0042 0.0000  2.9      98
     80000000   2.9583E-05 0.0039 0.0000  3.4      98
     90000000   2.9587E-05 0.0037 0.0000  3.5      98
    100000000   2.9565E-05 0.0035 0.0000  3.8      98
 ************************************************************************************************************************
 dump no.    2 on file runtpe     nps =   100000000     coll =        2875428     ctm =      835.77   nrn =
 2896106830
 run terminated when   100000000  particle histories were done.
 computer time =  872.06 minutes
 mcnp     version 6.mpi 07/01/21                    06/04/22 09:34:25                    probid =  06/04/22 09:24:05
```

APPENDIX C

Table C.1. MCNP® data and calculated dose rates for the straight lead tunnel configuration

Distance (cm)	pSv/p (Tunnel)	pSv/p (Free Air)	pSv/h (Tunnel)	pSv/h (Free Air)	mSv/h (Tunnel)	mSv/h (Free Air)
10	9.72E-03	4.35E-03	9.90E+11	4.43E+11	9.90E+02	4.43E+02
15	2.23E-03	1.91E-03	2.27E+11	1.94E+11	2.27E+02	1.94E+02
20	1.57E-03	1.16E-03	1.60E+11	1.19E+11	1.60E+02	1.19E+02
25	9.06E-04	8.64E-04	9.23E+10	8.80E+10	9.23E+01	8.80E+01
30	6.85E-04	6.61E-04	6.98E+10	6.74E+10	6.98E+01	6.74E+01
35	4.09E-04	3.92E-04	4.17E+10	3.99E+10	4.17E+01	3.99E+01
40	3.19E-04	2.68E-04	3.25E+10	2.73E+10	3.25E+01	2.73E+01
45	2.28E-04	2.10E-04	2.32E+10	2.14E+10	2.32E+01	2.14E+01
50	1.89E-04	1.78E-04	1.93E+10	1.82E+10	1.93E+01	1.82E+01
55	1.51E-04	1.47E-04	1.54E+10	1.50E+10	1.54E+01	1.50E+01
60	1.25E-04	1.14E-04	1.27E+10	1.16E+10	1.27E+01	1.16E+01
65	9.93E-05	9.77E-05	1.01E+10	9.95E+09	1.01E+01	9.95E+00
70	8.88E-05	8.42E-05	9.05E+09	8.58E+09	9.05E+00	8.58E+00
75	7.51E-05	7.32E-05	7.65E+09	7.45E+09	7.65E+00	7.45E+00
80	6.42E-05	6.51E-05	6.54E+09	6.63E+09	6.54E+00	6.63E+00
85	5.48E-05	5.94E-05	5.58E+09	6.05E+09	5.58E+00	6.05E+00
90	5.14E-05	5.48E-05	5.24E+09	5.59E+09	5.24E+00	5.59E+00
95	4.60E-05	5.01E-05	4.69E+09	5.11E+09	4.69E+00	5.11E+00
100	3.49E-05		3.56E+09		3.56E+00	

Table C.2. MCNP® data and calculated dose rates for the straight concrete tunnel configuration

Distance (cm)	pSv/p (Tunnel)	pSv/p (Free Air)	pSv/h (Tunnel)	pSv/h (Free Air)	mSv/h (Tunnel)	mSv/h (Free Air)
10	1.01E-02	4.80E-03	1.03E+12	4.89E+11	1.03E+03	4.89E+02
15	2.50E-03	2.29E-03	2.55E+11	2.34E+11	2.55E+02	2.34E+02
20	1.79E-03	1.45E-03	1.82E+11	1.48E+11	1.82E+02	1.48E+02
25	1.08E-03	1.04E-03	1.10E+11	1.06E+11	1.10E+02	1.06E+02
30	8.27E-04	7.97E-04	8.43E+10	8.12E+10	8.43E+01	8.12E+01
35	5.06E-04	4.45E-04	5.16E+10	4.53E+10	5.16E+01	4.53E+01
40	3.94E-04	2.93E-04	4.01E+10	2.98E+10	4.01E+01	2.98E+01
45	2.82E-04	2.28E-04	2.87E+10	2.33E+10	2.87E+01	2.33E+01
50	2.33E-04	1.94E-04	2.37E+10	1.98E+10	2.37E+01	1.98E+01
55	1.84E-04	1.60E-04	1.87E+10	1.63E+10	1.87E+01	1.63E+01
60	1.51E-04	1.25E-04	1.54E+10	1.27E+10	1.54E+01	1.27E+01
65	1.18E-04	1.06E-04	1.20E+10	1.08E+10	1.20E+01	1.08E+01
70	1.05E-04	9.19E-05	1.07E+10	9.36E+09	1.07E+01	9.36E+00
75	8.81E-05	7.98E-05	8.98E+09	8.13E+09	8.98E+00	8.13E+00
80	7.45E-05	7.09E-05	7.59E+09	7.23E+09	7.59E+00	7.23E+00
85	6.29E-05	6.47E-05	6.41E+09	6.59E+09	6.41E+00	6.59E+00
90	5.87E-05	5.97E-05	5.98E+09	6.08E+09	5.98E+00	6.08E+00
95	5.23E-05	5.45E-05	5.33E+09	5.56E+09	5.33E+00	5.56E+00
100	3.96E-05		4.03E+09		4.03E+00	

Table C.3. MCNP® data and calculated dose rates for the straight iron tunnel configuration

Distance (cm)	pSv/p (Tunnel)	pSv/p (Free Air)	pSv/h (Tunnel)	pSv/h (Free Air)	mSv/h (Tunnel)	mSv/h (Free Air)
10	1.01E-02	4.66E-03	1.03E+12	4.75E+11	1.03E+03	4.75E+02
15	2.48E-03	2.14E-03	2.53E+11	2.18E+11	2.53E+02	2.18E+02
20	1.77E-03	1.33E-03	1.80E+11	1.36E+11	1.80E+02	1.36E+02
25	1.05E-03	9.72E-04	1.07E+11	9.91E+10	1.07E+02	9.91E+01
30	7.99E-04	7.45E-04	8.14E+10	7.59E+10	8.14E+01	7.59E+01
35	4.82E-04	4.28E-04	4.92E+10	4.36E+10	4.92E+01	4.36E+01
40	3.74E-04	2.88E-04	3.81E+10	2.93E+10	3.81E+01	2.93E+01
45	2.66E-04	2.24E-04	2.71E+10	2.29E+10	2.71E+01	2.29E+01
50	2.20E-04	1.91E-04	2.25E+10	1.94E+10	2.25E+01	1.94E+01
55	1.75E-04	1.57E-04	1.78E+10	1.60E+10	1.78E+01	1.60E+01
60	1.44E-04	1.22E-04	1.46E+10	1.24E+10	1.46E+01	1.24E+01
65	1.13E-04	1.04E-04	1.15E+10	1.06E+10	1.15E+01	1.06E+01
70	1.00E-04	8.98E-05	1.02E+10	9.15E+09	1.02E+01	9.15E+00
75	8.44E-05	7.80E-05	8.60E+09	7.95E+09	8.60E+00	7.95E+00
80	7.17E-05	6.94E-05	7.30E+09	7.07E+09	7.30E+00	7.07E+00
85	6.08E-05	6.33E-05	6.19E+09	6.45E+09	6.19E+00	6.45E+00
90	5.68E-05	5.84E-05	5.79E+09	5.95E+09	5.79E+00	5.95E+00
95	5.07E-05	5.34E-05	5.16E+09	5.44E+09	5.16E+00	5.44E+00
100	3.83E-05		3.90E+09		3.90E+00	

Table C.4. MCNP® data and calculated dose rates for the curved tunnel configuration

Pathlength (cm)	pSv/p	pSv/h	mSv/h
75	2.93E-05	2.99E+09	2.99E+00
100	9.21E-07	9.38E+07	9.38E-02
125	1.15E-07	1.17E+07	1.17E-02

Table E.5. MCNP® data and calculated dose rates for the Cs-137 ZAB configuration

Position (10 m from walkway intersection)	pSv/p	pSv/h	mSv/h	µSv/h
Near Wall	1.73E-09	2.30E+07	2.30E-02	2.30E+01
Mid tunnel	2.58E-09	3.43E+07	3.43E-02	3.43E+01
Far wall	2.95E-09	3.93E+07	3.93E-02	3.93E+01

Table C.6. MCNP® data and calculated dose rates for the Co-60 ZAB configuration

Position (10 m from walkway intersection)	pSv/p	pSv/h	mSv/h	µSv/h
Near Wall	4.19E-09	5.58E+07	5.58E-02	5.58E+01
Mid tunnel	6.34E-09	8.45E+07	8.45E-02	8.45E+01
Far wall	7.45E-09	9.93E+07	9.93E-02	9.93E+01